The Dissertation Committee for Xinzhou Tan
certifies that this is the approved version of the following dissertation:

Magnetic Force Microscope study on high-anisotropy UMn_2Ge_2 and construction of a Spin Polarized Scanning Tunneling Microscope

Committee:

Alex de Lozanne, Supervisor

Alex Demkov

Jianshi Zhou

Maxim Tsoi

Zhen Yao

Magnetic Force Microscope study on high-anisotropy UMn_2Ge_2 and construction of a Spin Polarized Scanning Tunneling Microscope

by

Xinzhou Tan,

DISSERTATION

Presented to the Faculty of the Graduate School of

The University of Texas at Austin

in Partial Fulfillment

of the Requirements

for the Degree of

DOCTOR OF PHILOSOPHY

THE UNIVERSITY OF TEXAS AT AUSTIN

August 2017

Dedicated to the wondrous world.

Acknowledgments

First, I would like to thank professor de Lozanne for accepting me as a graduate student and introducing me into the scanning probe microscope world, where I have tons of fun. I benefit from his wisdom, humor, and sometimes even food! I will never forget his support and encouragement when I encountered difficulties. His insight on experimental physics and his encouragement to pursue simplicity surely have left long term impact on me.

Second, I would like to thank the former group members, including Neliza Leon-Brito, Morgann Berg, and Leujen Chen. Among them, Neliza graduated shortly after I joined this group. Nevertheless, I benefited from the experimental setup she had worked on, and her amazing hand-written notebook. I hope she is doing well in her current endeavors. Morgann was the senior student who taught me about the operation of the magnetic force microscope. She is brilliant and an excellent teacher, who was always patient to answer questions I had and gave me advice on many things. I wish her the best of luck with everything. Leujen Chen was working on the scanning tunneling microscope when I joined. Besides learning the basic operation of the STM from him, we also shared many interests in culture and history. I hope everything goes well for him!

Next, I would like to thank my fellow undergraduate lab mates. As

for the latter half of my graduate work, they are the best assistants and great company. Including Fernando, Francisco, Jorge, and Nathan. Especially, Jorge and Nathan contributed a great deal for etching STM tips and some of MFM work. Finally, this summer I had help from our high school scientists (Madeline, Alex and Andrei) with STM tips and editorial corrections. I wish all of them the best of luck in the future.

I would like thank professor Alex Demkov, professor Jianshi Zhou, professor Maxim Tsoi and professor Zhen Yao, who served as committee members in my advancement towards the PhD candidacy and who served again as members in my PhD defense committee. I am indebted to them for their offering of kind help and encouragement during my study as a graduate student, and for spending their time reading and correcting this thesis.

I appreciate Ed's extensive help in the cryogenics shop. I met with him almost every other day for refilling liquid nitrogen. I also want to thank Jack for his guidance in machining parts in the student shop, Kenny for his help on welding and Allan for his assistance whenever needed.

Finally, I acknowledge my family. Without them, I would never have possibly come this far, thank you!

Magnetic Force Microscope study on high-anisotropy UMn_2Ge_2 and construction of a Spin Polarized Scanning Tunneling Microscope

Publication No. _____

Xinzhou Tan, Ph.D.
The University of Texas at Austin, 2017

Supervisor: Alex de Lozanne

The first part of this dissertation introduces the theoretical background for the Magnetic Force Microscope (MFM), the Spin Polarized Scanning Tunneling Microscope (SP-STM), and the theoretical basis for magnetic domains. The second part addresses issues on the design and construction of a low temperature magnetic force microscope (LT-MFM) and its operation. The third part focuses on the LT-MFM experimental investigation on ternary UMn_2Ge_2 crystals. The forth part describes the construction and implementation of a low temperature SP-STM system.

Scanning probe microscopy (SPM), beginning with the invention of the STM, was first developed to study the electronic properties of different materials, such as imaging high T_c superconductors. But soon, as the SPM family

expanded, some of them developed into powerful techniques to characterize magnetic features. This category includes MFM and SP-STM. The former was widely used for imaging surface magnetic properties from hundreds of micrometers down to the nanometer scale, ideal for imaging magnetic domains. With our homemade LT-MFM system, we studied UMn_2Ge_2 single crystals, in which both the Uranium and Manganese atoms are magnetic. Flower-like magnetic domain pattern were found at room temperature, and they persisted all the way down to low temperature. Around 150K, Uranium atom ordering was revealed in the form of magnetic domain wall jumps, by partially saturating the sample and warming it up in zero field. In addition, the underlying mechanism of the flower pattern was explained using the domain branching scheme. On the other hand, a Low temperature SP-STM (LT-SP-STM) was designed and constructed, paving the way for spin mapping at the atomic scale thus characterizing magnetic materials with ultra-resolution.

Table of Contents

List of Figures

Chapter 1

Introduction

In 1981[1], the invention of the scanning tunneling microscope (STM) brought atoms within the reach of human vision. For the first time, atoms were directly imaged, and no longer only existed in equations and speculations. While this development strongly boosted material science research, the STM also inspired the further development of a series of characterizing tools which have been greatly expanding the horizons of human beings. Widely named "scanning probe microscopes", these instruments follow more or less the same principle of operation: a sensor, as small as possible is brought as close as possible to a sample surface to spatially resolve its various properties with ultra high resolution. Prominently, shortly after the development of the STM, the atomic force microscope, the second member of this family, was invented by Binning and Quate in 1986[2]. Shortly after, a variety of techniques, including the magnetic force microscope, was introduced. A few years later, a spin polarized version of STM was demonstrated in 1990[3]. Particularly with the latter two techniques, many experimental investigations on various magnetic materials became available, and further theories such as magnetic domain theory could be tested in much more resolved detail. Benefiting from the power of these tools, the research presented in this thesis will first deal with the nature

of these techniques, and theories of the interactions between the probes and the sample. These are indispensable for understanding the experimental data. A brief description of the basic energies involved in the magnetic properties of materials is also given in this chapter.

1.1 Theoretical Description of the Magnetic Force Microscope

The Magnetic Force Microscope (MFM) was developed as a modification of the Atomic Force Microscope (AFM); the latter was a solution to replace the scanning tunneling microscope for the imaging of insulating surfaces. As it is well known, the invention of scanning tunneling microscope (STM) marked the advent of the so-called scanning probe microscopy (SPM) family, which realized for the first time the power of atomic scale imaging. However, the STM is only applicable on conductive surfaces in order to carry a tunneling current. The atomic force microscope, however, senses the force between the cantilever tip and the surface, which can be applied to non-conductive materials. In 1991, Franz J. Giessibl et al[4] used it successfully to achieve atomic resolution, demonstrating tremendous potential for imaging all materials at the atomic scale. At the same time, variations of the atomic force microscope started to flourish, among them the Magnetic Force Microscope[5], generally realized by magnetically coating the tip, became one of the most used local magnetic probes.

The fundamentals of the MFM, which are the same as those of the

atomic force microscope and many other physics systems, take advantage of the harmonic oscillator model. A cantilever with a tip at the end, within a force field that only affects the tip, can be described well with the equation below:

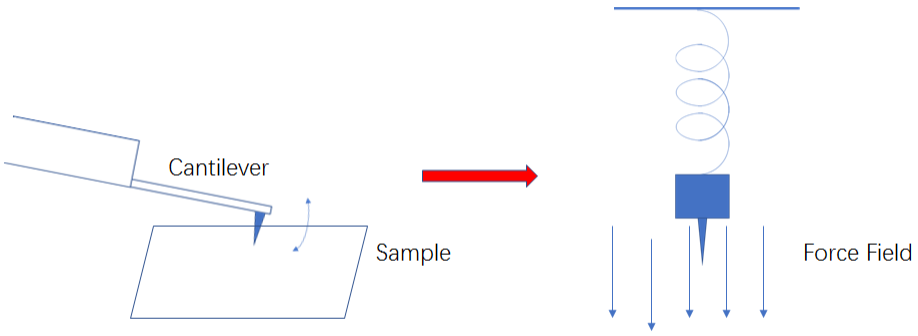

Figure 1.1: Cantilever modeled as a harmonic oscillator.

$$\frac{\partial^2 Z}{\partial^2 t} + 2\delta\frac{\partial Z}{\partial t} + \omega_0^2 Z = A_0 \cos\Omega t + F_{ex} \tag{1.1}$$

where Z is the displacement of the tip, δ presents the dissipation term, $\omega_0 = \sqrt{k/m}$ is the natural resonant frequency if without damping term and k is the hook constant, $A_0 \cos\Omega t$ represents the driving force term, and F_{ex} denotes the external force field which is a function of displacement. In order to simplify this expression into a standard second order differential equation, we linearize the external force field term into:

$$F_{ex} = F_{ex}(Z_0) + \frac{\partial F_{ex}}{\partial Z}(Z_0) + O(Z_0) \tag{1.2}$$

We only keep the first two low order terms, and by properly choosing Z_0, we replace Z by $Z - Z_0$. Then Equation 1.1 becomes the standard one:

$$\frac{\partial^2 Z}{\partial^2 t} + 2\delta\frac{\partial Z}{\partial t} + \omega^2 z = A_0 \cos\Omega t \tag{1.3}$$

where ω is the effective new natural resonant frequency, and the standard solution for the equation is:

$$Z(t) = Z_d(t) + Z_a \cos\Omega t + \Phi \tag{1.4}$$

The first term is the damping term that goes to zero as time goes to infinity, while the second term obeys the following expression:

$$Z_a = \frac{Z_{max}\omega/\Omega}{\sqrt{1 + Q^2(\omega/\Omega - \Omega/\omega)^2}} \tag{1.5}$$

$$\tan\phi = \frac{\omega_0\Omega}{Q(\Omega^2 - \omega^2)} \tag{1.6}$$

Where $Q = \omega_0/2\delta$ characterize the rate of energy transform in a system. The resonant frequency within the force field is $\tilde{\Omega}_r$:

$$\tilde{\Omega}_{rn} = \omega\sqrt{\Omega_r^2 - \frac{\omega^2 F'_{ts}}{k}} \tag{1.7}$$

and the frequency shift $\Delta\Omega$ relative to original resonant frequency without external force field Ω_r is:

$$\Delta\Omega = \Omega_r(\sqrt{1 - \frac{\omega^2}{k\Omega_r^2}F_{ts}^{'}} - 1) \tag{1.8}$$

Approximately, when $|\frac{\omega^2}{k\Omega_r^2}F_{ts}^{'}| << 1$, this becomes:

$$\Delta\Omega \approx \frac{\omega^2}{k\Omega_r^2}F_{ts}^{'} \tag{1.9}$$

Thus we find that the frequency shift is approximately proportional to the force gradient. A positive shift is obtained for a repulsive force, and a negative shift for an attractive force. For a magnetic force microscope, this external force field comes from the interaction between the magnetic coating on the tip and the magnetic field from the sample.

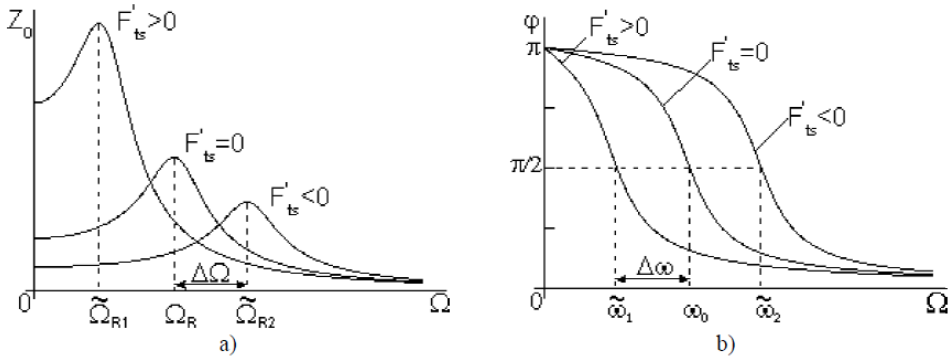

Figure 1.2: Resonant frequency (a) and phase shifts (b) of a cantilever in an external force field [6].

As implied in the equation, there would also be a phase shift, which under the approximation of $|\frac{k}{Q}F_{ts}^{'}| >> 1$ is:

$$\Delta\varphi \approx -\frac{Q}{k}F_{ts}^{'} \tag{1.10}$$

which is also proportional to the force gradient. Both the resonant frequency shift and the phase shift are shown in examples illustrated in Figure.1.2. In our system, we probe the magnetic domains on the sample by detecting the frequency shift.

By performing two scans: the first scan runs in tapping mode working as normal AFM in order to acquire the topographic image and the second scan runs in a lift mode, which keeps a constant distance between the tip and sample surface through retracing the first scan. The variation in the force gradient during the second scan reflects the magnetic features of the sample surface.

However, in order to fully interpret the data, it is not enough to only know the force, but one also needs the information of the magnetic coating on the tip in order to calculate the magnetic field generated by the sample. The strict way is of course to integrate the interaction between the magnetic moment of the tip and the magnetic field over the volume of magnetic coating:

$$U = \int_{tip} \vec{m}_{tip} \cdot \vec{B} d\vec{r} \tag{1.11}$$

and

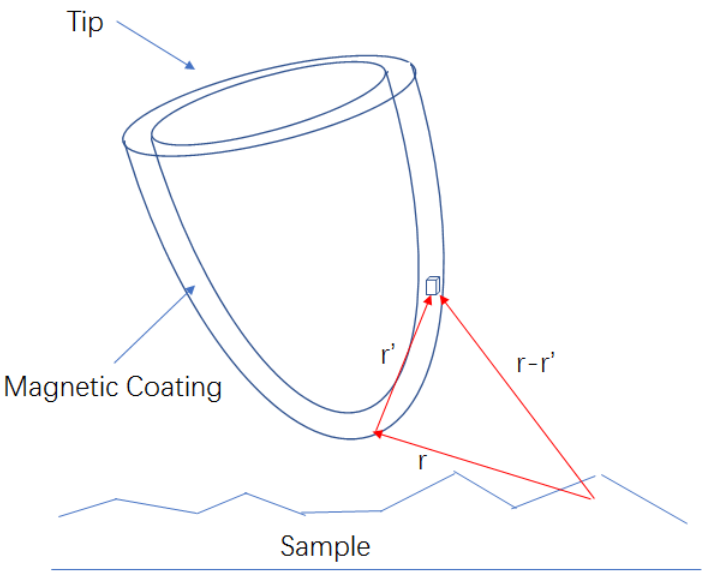

Figure 1.3: MFM tip and sample interaction.

$$\vec{F} = -\nabla U \tag{1.12}$$

From these formulas, in principle, we can extract magnetic field information. For a magnetic tip, by considering the extended geometry of a probe or coating, one can model the tip as a homogeneously magnetized prolate spheroid of suitable dimensions [7]. For tips with a magnetic coating, some other models were developed. Though far more realistic, these methods require much more effort and are highly dependent on the geometry of each individual tip, which in practice is often inaccessible. One alternative way is to simplify the magnetic coated tip as a point probe with both monopole q

and dipolar component $\vec{m}$. The force effectively is:

$$\vec{F} = \mu_0(q + \vec{M} \cdot \nabla)\vec{H} \tag{1.13}$$

Further if treat the tip only as a point dipole with tip magnetization M perpendicular to the surface, we will have:

$$U = -\int_{tip} \frac{\vec{M}(\vec{r})}{V_{tip}} \cdot \vec{B} d\vec{r} = -M_z B_z(\vec{r}_{tip}) \tag{1.14}$$

and

$$F = -\nabla U = M_z \frac{\partial B_z}{\partial z}(\vec{r}) \tag{1.15}$$

Though we oversimplified it by assuming that the tip moves only in the z direction (perpendicular to the surface), we extract usefully information the frequency shift is approximately proportional to the second derivative of the z-component magnetic field.

1.2 Theory of the Spin-Polarized Scanning Tunneling Microscope

The operating principle of the Spin-Polarized Scanning Tunneling Microscope (SP-STM) is mostly the same as that of the Scanning Tunneling Microscope (STM), except for additional considerations regarding the spin degree of freedom. The principle of the STM can be explained based on a perturbative approach in a one dimensional tunneling model. When the STM tip approaches the sample, the process can be treated as turning a sample

potential on and off, adiabatically. The approximation reasonable because the electrons in the tip move on a femotosecond timescale, much faster than tip motion during approaching. Wave function of electron in the tip follows the time dependent Schrodinger function:

$$-i\hbar\frac{\partial^2\phi}{\partial^2 z} + U_T + U_S = i\hbar\frac{\partial\phi}{\partial z} \tag{1.16}$$

Where:

$$U_T = e^{-\eta t} \tag{1.17}$$

and η is assumed very small to present the slowly turning on of tip potential. The state of the whole system including the tip and sample is a linear combination of tip and sample eigenstates before the tip and sample get close.

$$\phi = a_\mu(t)\phi_\mu^S e^{-iE_\mu^S t/\hbar} + \sum_{\nu=1}^{\infty} b_\nu(t)\phi_\nu^T e^{-iE_\nu^T t/\hbar} \tag{1.18}$$

Inserting this expression into the Schrodinger equation and projecting the equation to one of the tip states, while considering the adiabatic approximation ($\frac{\partial a_\mu(t)}{\partial t} = 0$ and $a_\mu(t) = 1$), we will have:

$$i\hbar\frac{\partial b_\nu}{\partial t} = < \phi_\nu^T|U_T|\phi_\mu^S > e^{-i(E_\mu^S - E_\nu^T + i\eta)t/\hbar} + \sum_{k=1}^{\infty} b_\nu(t) < \phi_\nu^T|U_S|\phi_\mu^T > e^{-i(E_\mu^T - E_\nu^T)t/\hbar} \tag{1.19}$$

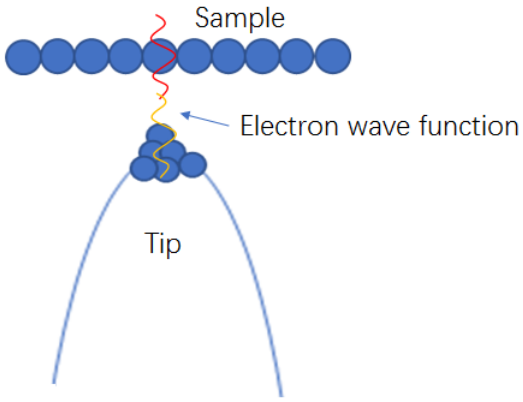

Figure 1.4: When tip and sample atoms become close enough, electrons start tunneling.

Neglecting the second order term, one can solve this equation by integrating over time:

$$|b_v(t)|^2 = \frac{e^{2\eta t/\hbar}}{(E_\mu^S - E_\nu^T)^2 + \eta^2}|M_{\mu\nu}|^2 \tag{1.20}$$

The tunneling matrix $M_{\nu\mu}$ is defined to represent $< \phi_\nu^T|U_S|\phi_\mu^S >$, which describes the probability of an electron originally at the sample state μ, tunneling to the tip state ν.The derivative of this with respect to time is the tunneling current from sample to tip.

$$P_{\mu\nu} = \frac{2\eta e^{2\eta t/\hbar}}{\hbar((E_\mu^S - E_\nu^T)^2 + \eta^2)}|M_{\mu\nu}|^2 \tag{1.21}$$

When $\eta \to 0$, this becomes

$$P_{\mu\nu} = \frac{2\pi}{\hbar}\delta(E_\mu^S - E_\nu^T)|M_{\mu\nu}|^2 \tag{1.22}$$

The current is given by $I_{\mu\nu} = eP_{\mu\nu}$, where e is the elementary charge. Following the same derivation, one can obtain the current from tip to sample $I_{\nu\mu}$. The last missing ingredients are the information about the energy states of tip ans sample: E_μ and E_ν. In solid state physics, for an example inside a crystal, not all energy are occupied by electrons, instead they occupy energy bands and follow fermi-dirac distribution. In addition, electrons only tunnel from occupied states to empty states. Thus, $P_{\mu\nu}$ must be modified by taking account of fermi-dirac distribution as:

$$P_{\mu\nu} = f(E_\mu^S - E_F^S)(1 - f(E_\nu^T - E_F^T))\frac{4\pi}{\hbar}\delta(E_\mu^S - E_\nu^T - eV)|M_{\mu\nu}|^2 \qquad (1.23)$$

where V is the bias, and E_F is the fermi energy of tip or sample. A factor of 2 is used to account for the spin degeneracy for a regular STM. The total current is obtained by summing all the states and subtracting the reverse current

$$I_{total} = \sum_{\mu\nu} I_{\mu\nu} - I_{\nu\mu} \qquad (1.24)$$

The summation over discrete states can be replaced by an integral over the density of states : $\sum \rightarrow \int n(E)dE$. Now, if assuming $|M_{\mu\nu}|^2$ is a constant $|M|^2$ regardless of the states, and at low temperature, the fermi-dirac distribution becomes a step function. This leads to:

$$I = \frac{4\pi}{\hbar} \int_0^{eV} d\epsilon n^T(E_F^T - eV + \epsilon) n^S(E_F^S + \epsilon) |M|^2 \tag{1.25}$$

and for small bias V, it becomes:

$$I = \frac{4\pi}{\hbar} V n^T(E_F^T) n^S(E_F^S) |M|^2 \tag{1.26}$$

Thus the tunneling current is proportional to density of states of the sample. The above derivation, however, is based on the approximation that the tunneling matrix $|M|$ is independent of energy, which is generally an over simplification. In order to calculate the tunneling matrix $|M|$, Tersoff and Hamann[8] proposed to treat the tip wave function to be s wave like. The s wave function decays exponentially, so only the very top atom at the tip matters. The resultant matrix element is:

$$M_{\mu\nu}(R_T) = C\phi_\mu^S(R_T) \tag{1.27}$$

R_T is the center of tip potential at the very apex and the current is:

$$I(R_T, V) = C' n_T \int_0^{eV} d\epsilon n^S(R_T, E_F^S + \epsilon) \tag{1.28}$$

C' is a constant and the integrand comes from $n^S(R_T, \epsilon) = \sum_\mu \delta(E_\mu^S - \epsilon)|\phi_\mu^S(R_T)|^2$. From Tersoff and Hamann's calculation, the tunneling current is proportional to the total local density of states of the sample within the

relevant energy window opened by the bias voltage. Further, if the window is small, we have approximately,

$$I(R_T, V) = C' V n_T n^S(R_T, E_F^S) \tag{1.29}$$

For SP-STM, a further constraint added is that electrons only go from occupied states to occupied states with the same spins. For a magnetic tip and magnetic sample, spins then play an essential role in the expression for the tunneling current. As the derivation is a straight forward extension of previous calculation, here only the final expression is shown :

$$I(R_T, V) = C''(n^T N^S(R_T, V) + m^T \cdot M^S(R_T, V)) \tag{1.30}$$

C'' is a constant, m^T is the magnetic density of states of the tip and M^S is the magnetic density of states of the sample.

1.3 Energies in Magnetic Domain Theory

Scanning probe techniques generally probe the surface properties of various materials. One of the purposes is to investigate phenomena stemming from the bulk, shedding light on the physics inside. As shown in previous sections, the physics of the probe mechanism is in principle well understood; still a good explanation of data obtained with a scanning probe microscope is often not straightforward.

Magnetic force microscope images, as an example, generally give the distribution of surface magnetic domains. However, it is not trivial to interpret

this surface domain image and determine the domain structure inside the sample. On one hand, as already can be seen in first section, the thickness and shape of the magnetic coating on the tip depends on the manufacturer, and is generally not easy to know in advance. On the other hand, more fundamentally, it is impossible to trace the magnetic field down to a unique magnetic structure without the extra guidance of theory.

Thus, a combination of assumptions and verifications, the so-called magnetic domain theory was developed to provide a valid description to compare with experimental data. The theory however are not powerful enough yet to replace experiment, and one part of the fact is it needs to be complex and diverse in order to fit different magnetic structures. This section will only introduce the most important energy terms for magnetic domain theory analysis.

1.3.1 Exchange Energy

Exchange energy is the most important term in magnetism. In the Heisenberg model, the exchange energy has the following expression:

$$E_{ex} = -\sum_{i,j} JS_i \cdot S_j \tag{1.31}$$

Where the sum covers all adjacent lattice sites, and J is the coupling constant.

1.3.2 Anisotropy Energy

As is well known, magnetic order originates from exchange energy between spins and can be explained by the above Heisenberg model. Further-

more, ferromagnetic energy also depends on the direction of magnetization relative to the structural axis, this anisotropic energy is due to the interaction between spins and the crystal field. Due to the symmetry properties of the crystal, an expansion in terms of spherical harmonics can be used to describe the most important contributions, and often only the lowest order terms are important, because the highest order terms may average out due to random spin fluctuations.

Here we present expression for the anisotropy energy for a cubic system and uniaxial system:

For cubic anisotropy, the lowest first, second, and third order terms are:

$$E_{kc} = K_{c1}(m_1^2 m_2^2 + m_1^2 m_3^2 + m_2^2 m_3^2) + K_{c2} m_1^2 m_2^2 m_3^2 \tag{1.32}$$

where m_1,m_2,m_3 are magnetization components along the cubic axis. In polar angle coordinates, this becomes:

$$E_{kc} = (K_{c1} + K_{c2} \sin^2\theta) \cos^4\theta \cos^2\phi \sin^2\phi + K_{c1} \sin^2\theta \cos^2\theta \tag{1.33}$$

As the anisotropy constants K_{c1} and K_{c2} change, the anisotropy surface may be quite complicated, such as Figure.1.5 shows. For uniaxial anisotropy, up to second order, the energy follows the expression:

$$E_{uc} = K_{u1} \sin^2\theta + K_{u2} \sin^4\theta \tag{1.34}$$

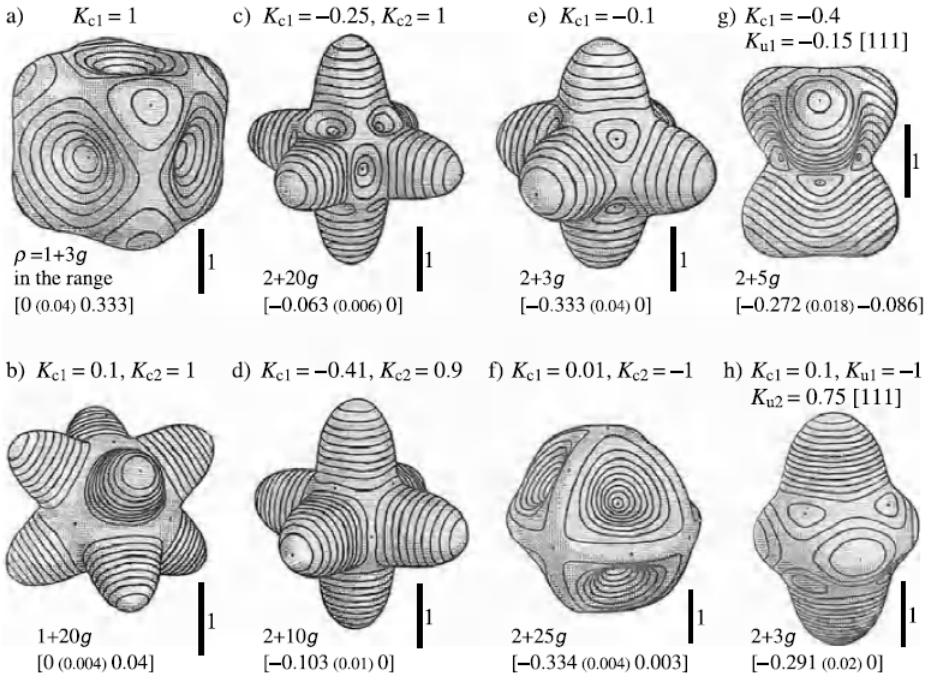

Figure 1.5: Different magnetic anisotropy energy surfaces for a cubic system[9].

For a constant energy surface, there will simply be two minima along the easy axis.

1.3.3 Domain Wall Energy

Besides the fundamental energy terms discussed above, here we discuss the energy of a particular structure: the magnetic domain wall. Magnetic domain walls separate magnetic domains with different spin orientation and often play an important role in the development of magnetic domain structure. Generally, there are two common wall types: Bloch wall and Neel wall.

For a Neel wall, at the wall the spins rotate perpendicular to the plane of the wall. For a Bloch wall, spins rotate in the plane of the wall, as figure.1.6 shows.

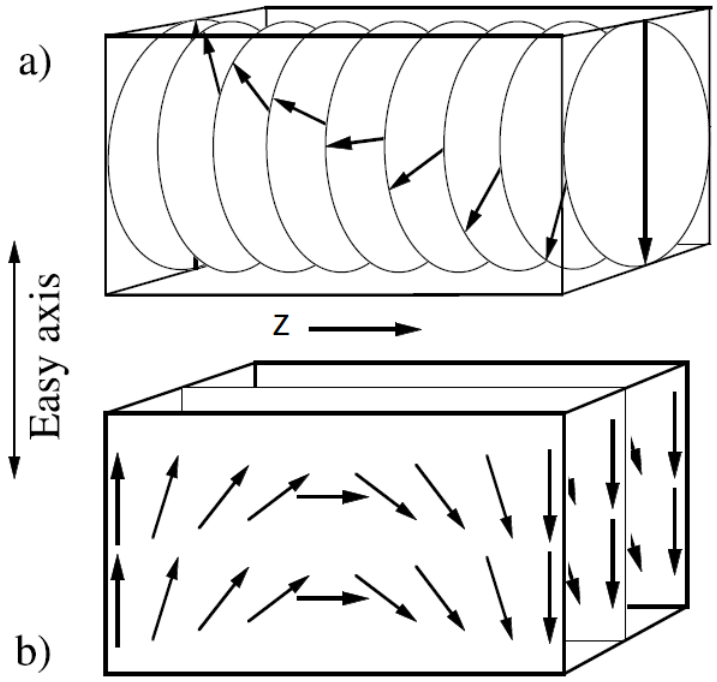

Figure 1.6: Magnetic Walls:(a)Bloch wall and (b)Neel wall [10].

For most bulk and large size samples, the Bloch wall is relevant, as the Neel wall is only common in very thin films. For the relevance of the research conducted in the thesis, the focus is energy and structure of a Bloch wall. The energy density of a domain wall is the sum of exchange energy and anisotropy energy, and the energy per unit wall area is the integral along the z direction:

$$\lambda_w = \int_{-\infty}^{\infty} A\frac{\partial\theta}{\partial z} + f(\theta)dz, \tag{1.35}$$

where A is the exchange constant and $f(\theta)$ presents the anisotropy energy. These two energies compete against each other, and $\theta(z)$ is the function to be determined in order to minimize the energy. By taking an infinitesimal displacement $\delta\theta$, we have:

$$\delta\lambda_w = \int_{-\infty}^{\infty} 2A\frac{\partial\theta}{\partial z}\frac{\partial\delta\theta}{\partial z} + \frac{\partial f(\theta)}{\partial z}\delta\theta dz \tag{1.36}$$

Integrate the first term by parts with the energy minimization condition $\delta\lambda_w = 0$

$$\int_{-\infty}^{\infty} -2A\frac{\partial^2\theta}{\partial^2 z} + \frac{\partial f(\theta)}{\partial z}\delta\theta dz = 0 \tag{1.37}$$

Then we have,

$$2A\frac{\partial^2\theta}{\partial^2 z} = \frac{\partial f(\theta)}{\partial z} \tag{1.38}$$

Through it, the following expressions can be obtained straightforwardly:

$$\lambda_w = \sqrt{A}\int \frac{1}{\sqrt{f(\theta)}}\,d\theta\ , \tag{1.39}$$

$$\delta_w = 2\sqrt{A}\int \sqrt{f(\theta)}\,d\theta. \tag{1.40}$$

besides the wall energy λ_w, and we also obtained the wall width δ_w, which is a measurable quantity in MFM experiments. One may keep in mind, all the

derivation above is based on the Heisenberg model, which may fail for itinerant magnetism. Nevertheless, it often gives a good qualitative understanding of the data.

Chapter 2

Low Temperature Magnetic Force Microscope Instrumentation

The basic design of a low temperature magnetic force microscope follows the scheme of all scanning probe microscopes. It consists of a scanner with an approaching mechanism, and a sensor with feedback loop to control the motion of the scanner. The emphasis of our setup is on low temperatures and the application of high external magnetic field.

The MFM system must be compact so it consumes less cryogens. Another reason for the compact design is that it needs to fit the inside of a superconductive magnet solenoid. The general design of MFMs usually consists of three types. The first one is the very common one: beam bounce structure [11], the laser is shot at the back of the cantilever through adjusting mirrors and is deflected to a photon detector. While this method is very popular in commercial AFMs, it complicates the instrumentation for low temperature use, since the alignment becomes difficult and electronic devices may not work. Other methods that are suitable for low temperature applications include those based on piezo resistive cantilever [12–14], tuning fork [15], fiber optic interferometers [17]. We adopt the latter method in our system simply

because the cantilever it uses is more commercially available. The schematic of the system is shown in the Figure.2.1.

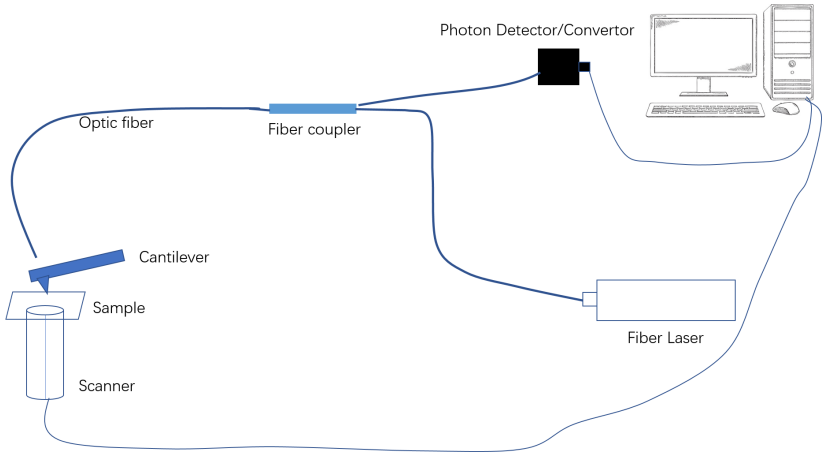

Figure 2.1: A simple schematic for an atomic force microscope.

2.1 Interferometer

The optic interferometer in our home-made MFM takes the advantage of a fiber laser, and most components can be placed outside the vacuum, thus greatly simplifying the instrumentation. The end of the optical fiber is placed several tens of micrometers away from the cantilever as the Figure.2.2 shows. The laser propagates through the input of a fiber coupler to the back of the cantilever and is reflected back through the original path and propagates out from the other output of the coupler. The reflected light from the cleaved surface of the fiber core and the reflected light from the back of the cantilever interfere with each other. The cantilever, fiber coupler and optical detector for-

m an optical interferometer. The fiber and cantilever distance D for maximas in the intensity of the interferometer will follow the expression:

$$D_{max} = (2n + 1)\frac{\lambda}{2} \tag{2.1}$$

Figure.2.2 shows a close look at the interferometer. As D changes continuously, the interferometer output follows a sinusoidal dependence and experiences multiple maximums and minimums, as Figure2.4 shows.

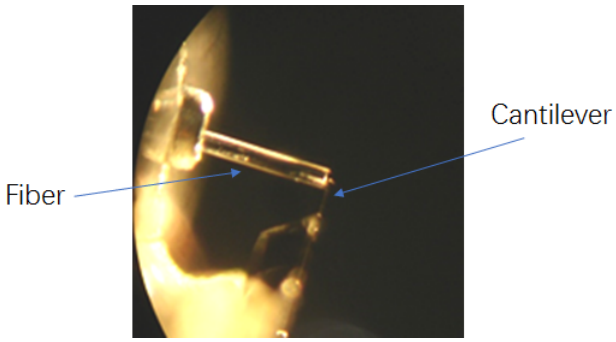

Figure 2.2: Optic microscope image of the interferometer.

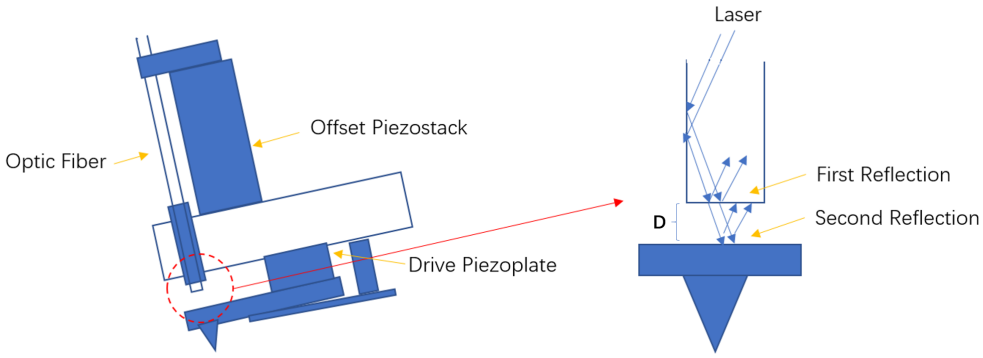

Figure 2.3: Schematics of interferometer.

An offset piezo stack as Figure.2.3 shows, is used to adjust the position of the fiber so as to control the offset distance D. The whole point of using the interferometer is to convert the vibration of the cantilever into an electrical signal. Clearly, the vibration of the cantilever changes D and leads to changes in interferometer signal. In practice, one only needs a small vibration on the cantilever, much smaller than the value of D, so that the amplitude of vibration δD is just a perturbation.

The next step is to simplify the relation between the amplitude of the vibration and the intensity of the interferometer output signal. As in Figure.2.4, we lock the interferometer right in the center of a fringe in the interferometer output. No matter which fringe the fiber is locked at, according to the equation D needs to be about an odd integer times the half wavelength of the laser, and the result is therefore the cantilever can vibrate approximately linearly within the range of the fringe curve as shown. In most of our experiments, the δD, amplitude of the cantilever is set so that the interferometer output is within 1/3 of the peak to peak intensity, where the response can be treated as mostly linear.

A homemade circuit, including a high voltage module and PI feedback control system, controls the offset piezo stack. It acquires the DC component of the voltage signal from the photon detector at the output of the interferometer, and compares it with the reference voltage setpoint, which is chosen by sweeping manually the interferometer fringe pattern. Then we lock the position of the fiber at the center of whichever fringe one prefers. On one hand,

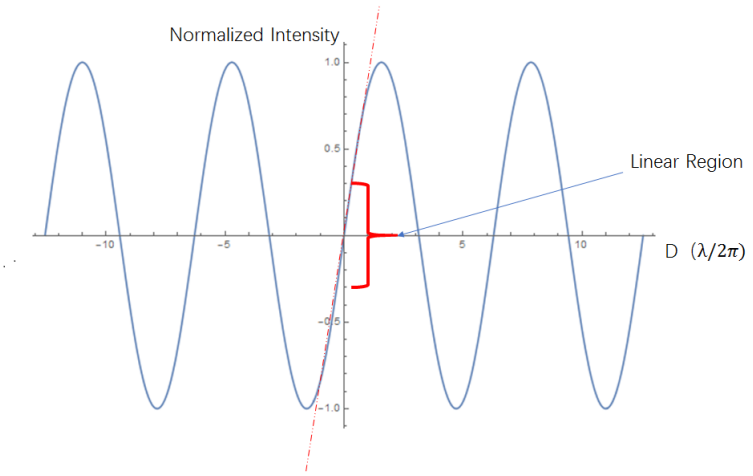

Figure 2.4: Fringes changes when distance 'D' between the end of the fiber and back of the cantilever.

one may notice a gradual decrease of peak to peak voltage as the fiber moves away from the cantilever, due to increasing loss of laser power at longer distance, so it is better to lock the fiber at the first fringe to maximize the signal. On the other hand, during coarse approach of the microscope, the motion of walker may generate enough vibration causing a big jump in the position of cantilever or fiber. Thus one wants to lock the fiber in the third or fourth fringe available, so that no matter which direction the D is changed, the piezo stack can always respond and lock the fiber back into the next available fringe.

2.2 Motion Control

The approach mechanism we choose to use is 'pan-type', namely stick-slip motion type which is most used in low temperature SPMs. Specifically, in

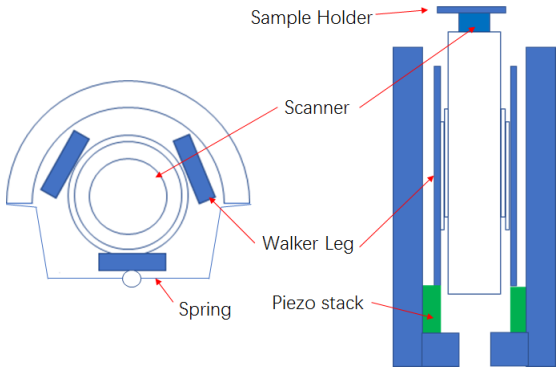

Figure 2.5: A simple schematic for the MFM body.

our MFM system, there are total three walker legs as the Figure.2.5 shows, and each of them is driven by a piezo stack to fire sequentially, producing overall motion for the scanner. Besides Z motion, there are also XY positioners, which

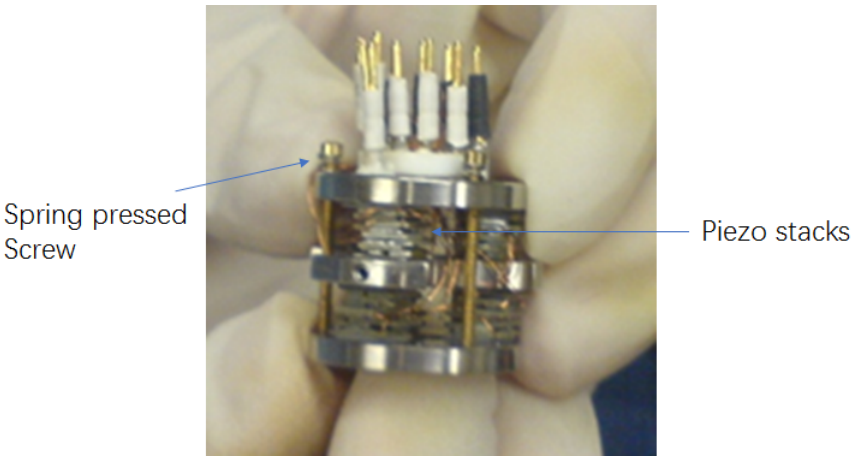

Figure 2.6: Lateral walkers. Cantilever and offset piezostack assembly attaches to the bottom of it.

are driven by 6 home made piezo stacks. For each piezo stack, there are 4 X direction shear piezo plates, and 4 Y direction piezo plates. The 6 walker legs

are independent and generate stick slip motion in the XY plane. Figure.2.6 shows a close look of the lateral walker assembly.

The lateral walking capability is essential for searching small devices. As an example, Figure.2.7 shows the process for finding a small topological insulator device with only a 10 um plus 10 um area, the green circle marks the target, and the yellow circle marks one of the reference points. With the walker design, the microscope shows excellent lateral mobility for finding small objects.

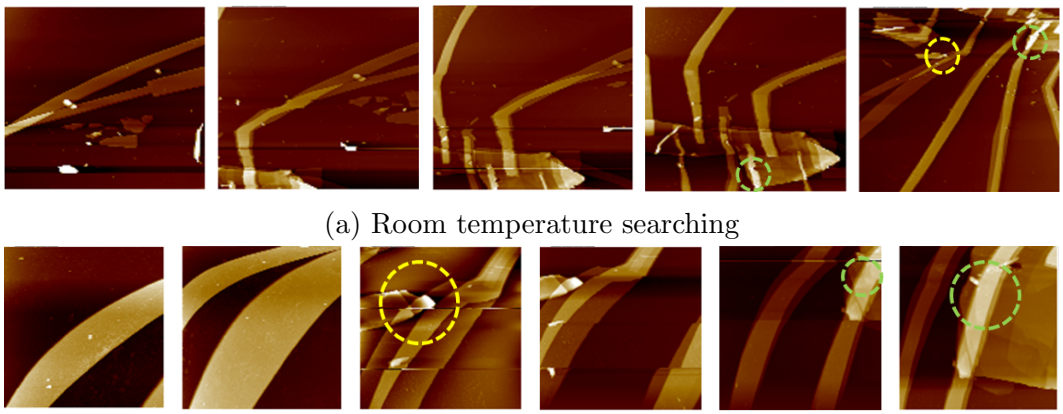

(a) Room temperature searching

(b) Low temperature searching

Figure 2.7: From left to right: process of searching a small topological insulator device first at room temperature then after cooled down to 77K. The green circle labels the device, and the yellow circle marks one of the features chosen as a reference point.

The disadvantage of the home made piezo stacks are that they are very hard to repair and need too many wires to assemble and control. For example, currently there are 12 control wires for lateral walkers. One of the

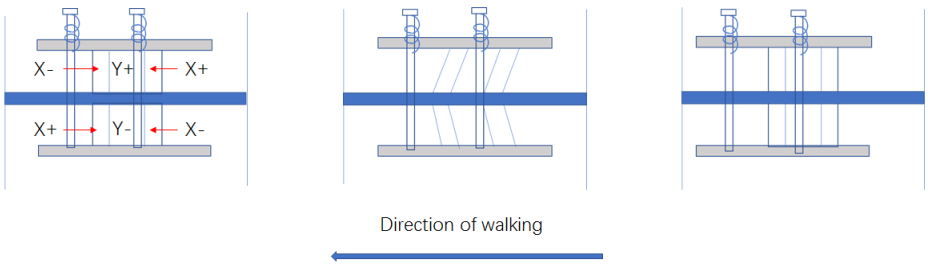

Figure 2.8: Schematic of our lateral walker design with scanners.

improvements that can be made is to replace the 6 walkers with two short tube scanner as seen by the schematics shown in Figure.2.8. Shorting X+ of one scanner with X- of another scanner, one can reduce the number wires to 4 wires. The mechanism of scanner driven stick slip motion is already realized and described in reference [16], which is successfully applied on both a Scanning Hall probe and a room temperature scanning tunneling microscope. A slightly different design from the previous 6 legs firing alternatively: two scanners fire together to produce jerky and slow motion.

2.3 Vacuum System and Thermal Exchange

To achieve low temperature, the microscope body is attached on an oxygen free, high conductivity (OFHC) copper rod, then installed into a pipe with 1.25 inch outer diameter. About an inch above the microscope body, there are two thick OFHC copper rings which fit tightly onto the rod and pipe, thus working as heat sink to cool down the system. Once the pipe is pumped down to low pressure, we insert it into a Kadel cryogenic helium

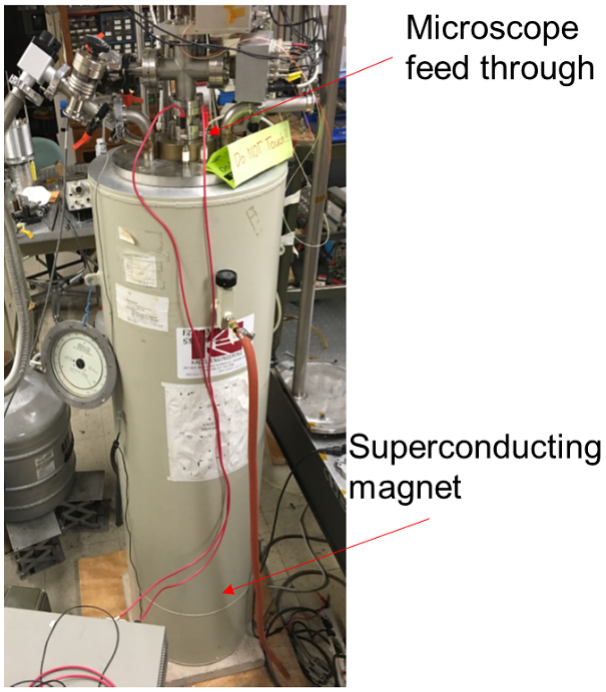

Figure 2.9: Magnetic Force Microscope System.

dewar. Between the pipe and the cryogen, there is an inter-layer jacket which usually is also pumped down, and it serves as a buffer to allow control of the heat transfer between the cryogen and the microscope by adjusting the pressure of exchange helium gas in it. Together with the heater on the sample stage, these mechanisms are used to control the temperature of the sample. At the bottom of the Kadel dewar a superconductive magnet is installed to provide a vertical magnetic field up to 8 tesla. The connections for the magnet are at the top of the dewar. A fiberglass tube all the way to the top covers the lead wires, which also work as a cold helium gas drain. This design cools the lead wire down and reduces the heat transfer through it.

The system usually is pumped at least continuously 24 hours before cooling down. Then, some pure Helium gas is transferred into the microscope. There are two things one needs to take care of in Helium gas transfer: First,

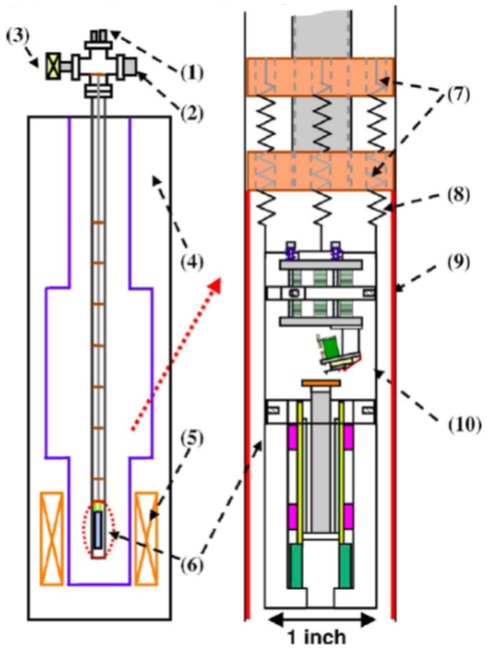

Figure 2.10: Left: Schematics of the Kadel dewar and the microscope vacuum system. Right: Schematics of the microscope body inside, description of the parts can be found in reference[17, 18].

one reason for putting helium gas into the microscope is to reduce the so called 'ringing' effects. At low pressure, the cantilever will be very sensitive to various excitations which are not damped quickly in high vacuum. As in equation above, it means that the first term cannot be ignored. On the other hand, this often weakens the microscope's capability to accurately trace the topography of a sample with a rough surface. For example, when the cantilever

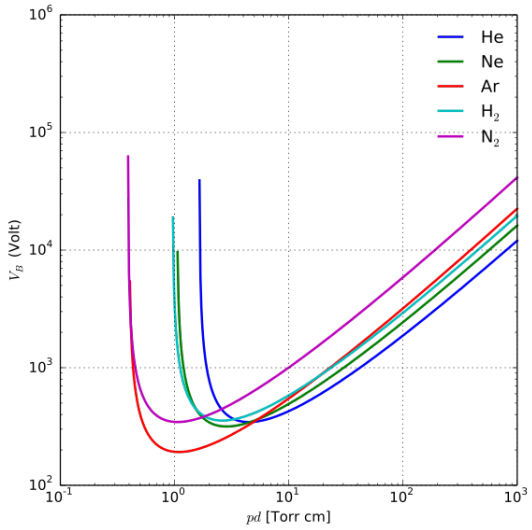

Figure 2.11: Paschen Law for different gases[19].

strikes a high feature, a quick reaction of the scanner and the rapid change of the force between tip and sample may bring multiple noisy frequencies that stay for a significant period of time, making surface tracing become difficult. As in MFM lift mode, the 'ringing' effect gives artificial magnetic signals at the beginning of trace scan, where the cantilever just landed from higher position thus is not stable. For this situation, a retrace scan and retrace lift scan is more accurate.

Second, once helium gas is put in, the pressure needs to be carefully chosen to avoid discharging inside the microscope. Discharging usually happens from the scanner electrodes, the voltage of which can reach as high as 440 volts. A discharging event can crash the tip and cause a drastic drop of the scanner. Theoretically, the breakdown discharging voltage follows the

Paschen's law as shown in the Figure.2.11. By experience, it's best keep pressure to be between 1 to 5 torr in order to avoid discharging and still reducing the 'ringing' effects.

Chapter 3

MFM Investigation on High Anisotropy UMn_2Ge_2

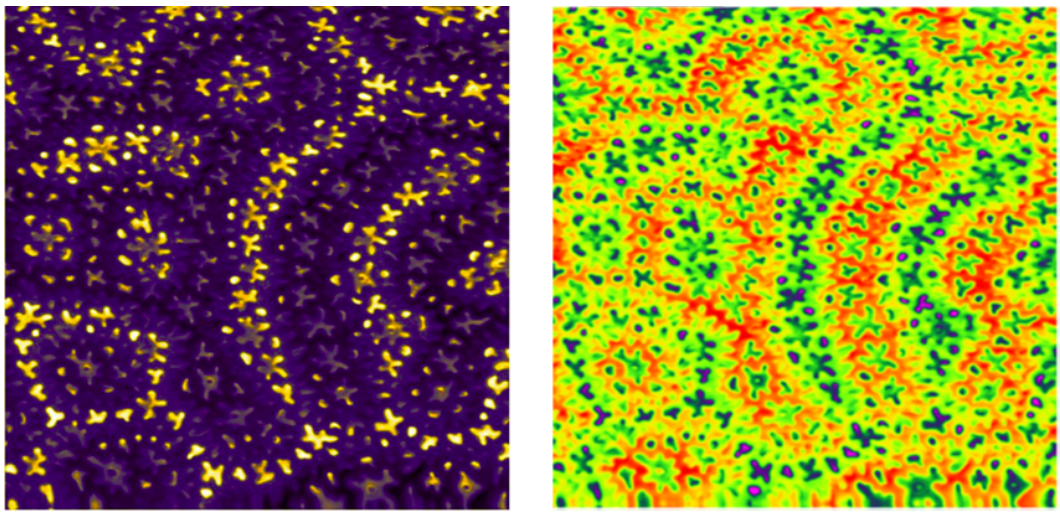

Figure 3.1: Flower-like pattern on UMn_2Ge_2 with two different color schemes.

UMn_2Ge_2 is a ternary compound belonging to the famous $ThCr_2Si_2$ type crystal structure family[20], as shown in Figure.3.2. This structure is well known for wide range of intriguing properties such as unconventional superconductivity[21, 22], for an example, the high T_c superconductor KFe_2Se_2. On the other hand, the composition of 5f uranium atom and 3d transition metal brings up competition of various energy terms that not only lead to novel

transport phenomena like superconductivity and heavy fermion behavior[23], but also rich magnetic properties ranging from antiferromagnetism to ferromagnetism and paramagnetism[24–27]. UMn_2Ge_2 among them is particular interesting as both uranium and manganese carry sizable magnetic moments.

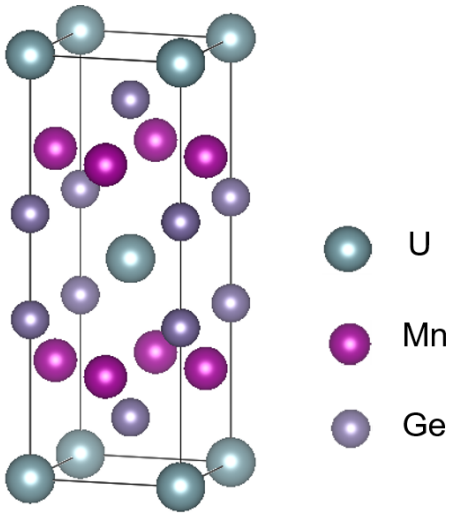

Figure 3.2: Lattice structure of $UMn2Ge2$.

Magnetization, neutron scattering, Kerr effects measurements indicated that the manganese atom ordering temperature is about 380K, and that the uranium atoms order at much lower temperature around 150K[28–30]. Recent SQUID measurements under high-pulsed magnetic field, as shown in the Figure.3.3, revealed a huge uniaxial anisotropy energy with an unusually large second order anisotropy constant, larger than that of the first order[31]. Remarkably, with high field up to 62 tesla along the c axis of the crystal, the sample still cannot reach saturation. To date, however, local and spatially resolved studies on the magnetic properties of this compound are still

lacking. All the previous researches then has raised questions like: What do the magnetic domains look like on this compound? How does the uranium atom ordering affect the domains as temperature changes? What is the nature of the remarkable high magnetic anisotropy? Fortunately, MFM offers us the opportunity to investigate these interesting questions in detail. With our homemade LT-MFM, not only are we able to image the magnetic structure on the nanometer scale, but also we can study the domain evolution with temperature and external magnetic field changes.

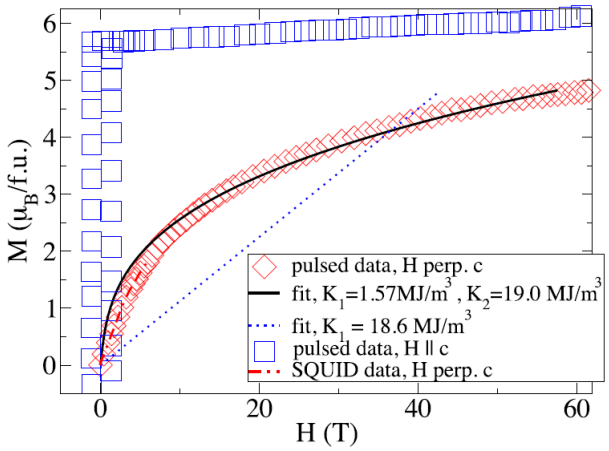

Figure 3.3: High-pulsed magnetic field experiment on a UMn_2Ge_2 single crystal[31].

3.1 Room Temperature Scan

UMn_2Ge_2 sample was prepared at Los Alamos National Lab. It was grown from elements of 99.9% purity in a molten Z_n flux. The reaction was

realized by loading elements with a particular ratio $1(U)$:$2(M_n)$:$20(Z_n)$ into a crucible[31], then heated to 600°C for 8 hours then held for another 6 hours. It is further heated to 1050°C for 8 hours and held at this temperature for 24 hours before cooling down to 650°C for 200 hours. With above substantial treatments, the single crystal platelets with millimeter side dimensions and thickness of 0.5mm to 1 mm were obtained. The particular sample we received was confirmed by Lauve diffractometry[33] to be consistent with the $ThCr_2Si_2$ crystal structure, and with the sample surface perpendicular to c axis of the crystal structure. However, some areas of the sample surface were rough, covered with irregular high features as seen in optical microscope images in Figure.3.4. Since the sample is too thin to cleave, it becomes difficult to perform MFM study, particular on rough area. Nevertheless, enough flat surface is still available after patiently adjusting the landing zone of the MFM tip. The top surface of the sample is tilted a little bit; generally, the topography is such that the height of the sample decreases from 0.5 mm in the rough area to a height of 0.3 mm in the smooth area.

As shown in the previous section, to obtain accurate magnetic mapping of the sample the surface topography must be first obtained. This is realized by the so-called tapping mode scanning. The cantilever is approached to the sample surface with a given set point amplitude. The set point amplitude is smaller than the free oscillation amplitude when the cantilever is far away from the sample. The initial value can be chosen to be 90% of the free oscillation amplitude, one can reduce the value so the cantilever is tapping 'harder' on the

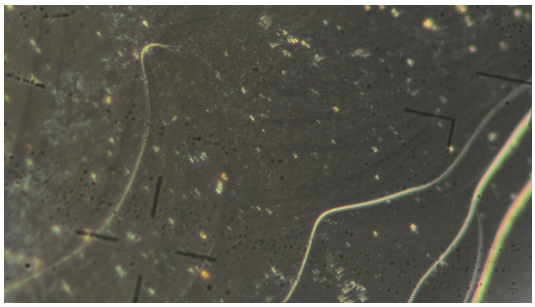

(a) Smooth area on the sample.

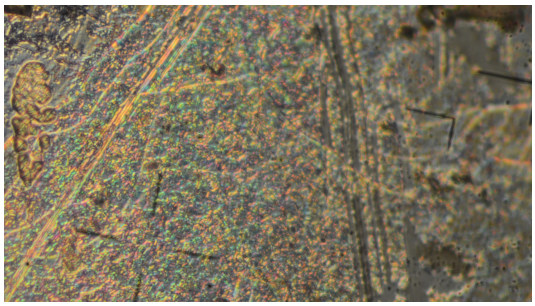

(b) Rough area on the sample

Figure 3.4: Optical microscope image of the sample surface.

surface and generally make the topography tracing more accurate, however, cantilever also will be worn out faster. In general, the tapping mode is better for protecting the cantilever and tip than the contact mode, in which cantilever tip is touching surface all the time, and this is especially true for rough surfaces like our sample. After tracing the surface, the tip is raised away from the surface to height about a hundred nanometers to perform a lift mode scan that strictly follows the previously obtained topography. We use low magnetic moment tip as we found that with regular tips the topography will be strongly correlated with magnetic feature thus leading to inaccurate magnetic imaging.

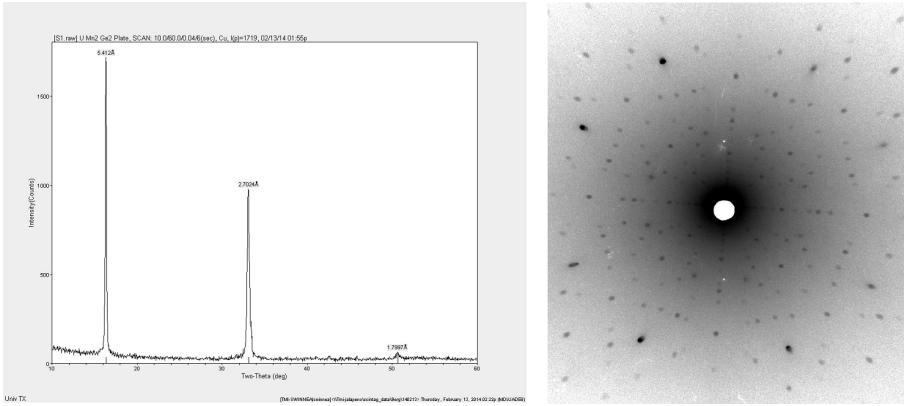

Figure 3.5: Laue diffraction data of UMn_2Ge_2[33].

This is a common problem with strong ferromagnets, such as $NdFeB$. A cantilever with a low moment has a weaker response to the magnetic force, making the scanning more stable.

We first performed a big area scan on the smooth surface area at room temperature and in air. The result is shown in Figure.3.6. The magnetic domains form flower-like patterns. There is also a maze of magnetic strip domains, decorated with bright magnetic domain flowers. The adjacent strip domains have different contrast and flower-like domains are in bright contrast relative to its surroundings. It is well known that this type of flower contrast is also reported on $NdFeB$ [34]. The combined kerr microscopy and MFM experiment on NdFeB revealed the magnetic pattern from MFM could be a combination of so called magnetic charge contrast and magnetic susceptibility contrast [35]. Specifically on UMn_2Ge_2, the magnetic field generated by the large strip domains is very strong that it is able to alter part of the mag-

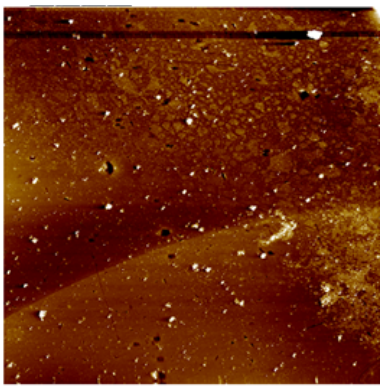

(a) Topography of the smooth area scan.

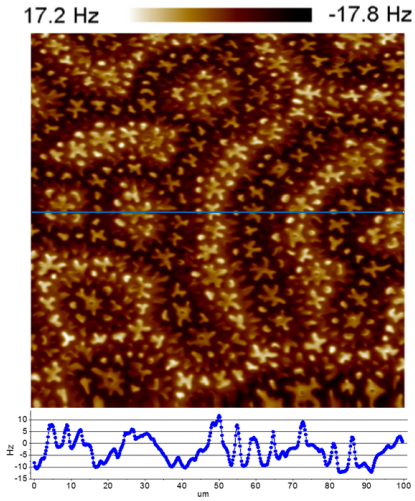

(b) Magnetic image of the smooth area scan.

Figure 3.6: ((a)Room temperature topography image on UMn_2Ge_2.(b)The corresponding magnetic domain pattern. Scan size: 100um*100um. Color scale corresponds to the resonant frequency shift that is directly proportional to the magnetic force gradient experienced by the MFM cantilever. The blue line in the center marks the position where the cross section is taken, vertical axis labels the resonant frequency shift.Negative frequency shifts corresponds to attractive force and positive frequency shift corresponds to repulsive force.

netization of the tip so the scanning can be treated as partial susceptibility imaging, and the re-alignment of the tip magnetization along strip domain magnetization effectively results in an attractive interaction and brings a negative resonant frequency shift to the cantilever. On the other hand, the bright flower-like domains developed inside strip domains are not able to strongly change the tip magnetization. As under the assumption the bright domain has different spin orientation from the surroundings, the interactions between tip and the flower would tend to be repulsive and thus brings up frequency

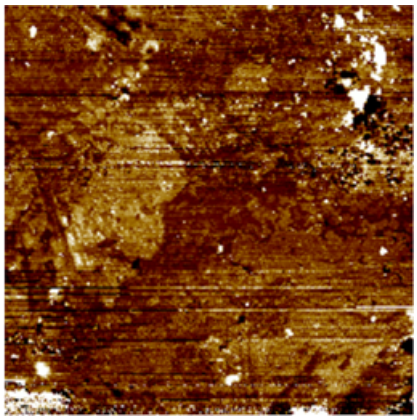

Figure 3.7: Topography corresponding to rough surface during zero field cooling down scan.

shift toward positive direction, consistently with the magnetic charge imaging. Thus similar with MFM data on $NdFeB$, the magnetic pattern contrast on UMn_2Ge_2 can be understood. This imaging mechanism is further illustrated in cross section plot in Figure.3.6(b) in terms of resonant frequency shifts. In addition, the contrast difference on different strips may also reflect the contribution from the room temperature remanence magnetic moment caused by spontaneous magnetization, for which inside the sample volume of magnetic domains with one spin direction is larger than that with opposite spin direction. By having performed scanning at much lower temperatures down to 77K, we found that the magnetic domain structure remains the same as the room temperature pattern, indicating that the uranium atom magnetic ordering is not able to alter the already existing magnetic domain shapes.

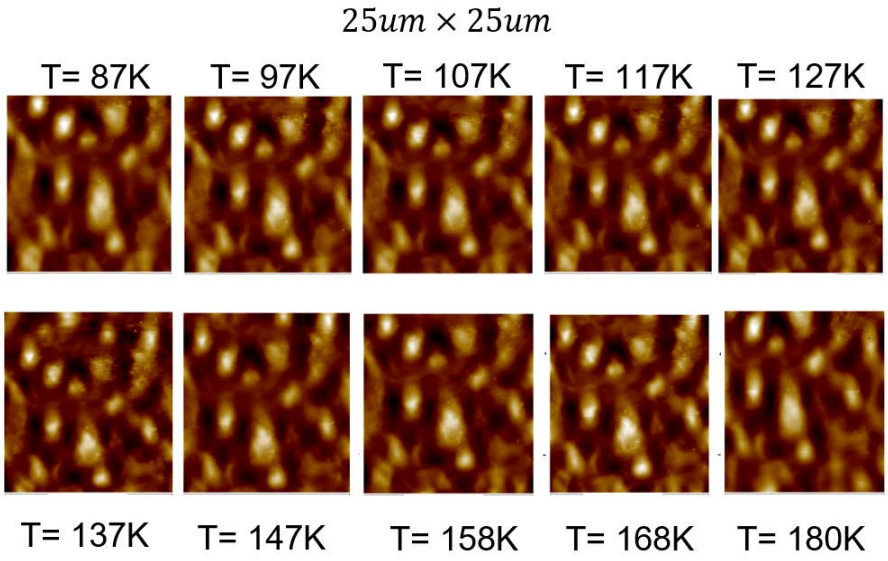

Figure 3.8: Zero-field cooling scan on a rough surface. Domains look round with a polished edge due to the random spike-like high features. However, the magnetic domain structure stays the same when the temperature goes down.

3.2 Uranium Atom Phase Transition

The Uranium magnetic phase transition in UMn_2Ge_2 has been observed and reported. One interesting question is how the phase would be reflected in the magnetic domain structure evolution and formation. We performed scanning while cooling zero field. Unfortunately the tip landed on a rough surface, and the topography is shown in Figure.3.8. The cooling was performed from 180K, across the temperature of the reported Uranium ordering temperature: 150K to 87K. We found randomly distributed round shape domains, as shown in the Figure, and little change with temperature. The irregular surface structures disturb the magnetic domains and destroy the

flowers-shaped domains. On a smooth area, and performing scans down to 77K, we found that the magnetic domain structure remains the same compared with the room temperature pattern, indicating that the uranium atom magnetic ordering is not able to alter the already existing shapes of the magnetic domains. The detailed formation of the domain patterns is particularly interesting, as described by the following experiment.

For further investigation of the evolution of the flower-like domains and for observing Uranium atom ordering directly through magnetic imaging, we first applied a one-tesla magnetic field perpendicularly to the sample, then we shut the magnetic field down and performed zero-field warming. The magnetic domain evolution was driven by thermal excitation of the domain walls. At a temperature around 60K the magnetic domains were partially saturated and big magnetic domains formed. The domain walls were clearly seen, however, the magnetic contrast difference between different domains was not as big as compared with the contrast in the domain wall area. To understand this, we recall that the domain wall separates adjacent domains with spins pointing in opposite directions. The weaker magnetic contrast between adjacent domains indicates that the magnetization of the tip was realigned and flipped on each domain, leading to an always-attractive interaction and less frequency shift difference. When the temperature goes up, the domain wall between big domains starts to twist and the major domains grow into each other. The bright domain starts to nucleate at low temperature and first appears to be strips, then grows into shapes that are more and more flower-like. During the warm-

ing up, there are several events brought about by Uranium atom ordering. At temperatures between 127K and 137K, there is a jump in a domain wall toward the domain above, around the upper right corner (marked by the green circle). In the meantime, a bright domain suddenly formed inside the expanded large domain. Moreover, at temperatures between 137K and 147K, the domain near the left side (the blue circle) experienced a sudden break. These unusual drastic events are well correlated the temperature range where U atoms order ferromagnetically, and similar events cannot be found outside of this range. In

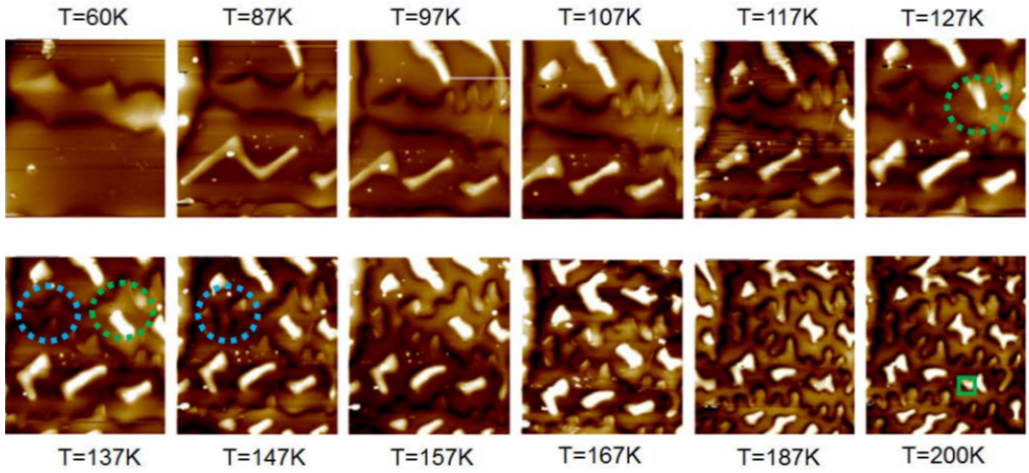

Figure 3.9: Evolution of magnetic domains during zero field warming. The sample was first cooled in zero field, then one tesla was applied and removed at around 40K, and finally the MFM data was taken at the temperatures shown. The scan size was maintained around 35um*35um with some fluctuations at higher temperatures. Color scale bars are not shown as absolute frequency shift is not essential, and it changes with temperature. The contrast is adjusted for each image to show how the domain walls evolve. The blue and green dashed circles label the area where a magnetic domain wall jumped and new bright domain broke apart due to the magnetic phase transition of the uranium atoms.

order to find further evidence for U atom ordering we took MFM images while cooling in zero field. However, this time we focused on a small area on a single domain sitting on the boundary between the big domain and a bright domain, marked with a small green square in Figure.3.9. The tip magnetization should stay unchanged through the whole series of scans and Figure.3.10 shows the magnetic images. We calculated the magnetic roughness as the rms value of the frequency shift over each image, which provides a quantitative comparison of the magnetic contrast. In Figure 3.11 we see that the magnetic roughness versus temperature changes rapidly around 150K, the temperature of Uranium moment ordering. Furthermore, the temperature range is consistent with that where drastic domain motion happens, as discussed above. This gradual, yet prominent U ferromagnetic transition has already been observed by previous investigations, but is the first local experimental evidence. Furthermore, the decrease of rms roughness with cooling means that the Uranium moments order in the opposite direction (antiferomagnetically) with respect to the already-ordered Manganese moments, as predicted by first principles calculations[31, 36]. The anti ferromagnetic coupling between U atom and Mn atom reduces the stray field of the magnetic domains as well as the magnetic dipole-dipole interaction between adjacent magnetic domains. This effectively weakens domain wall mobility.

In the zero-field warming experiment described above, the antiferromagnetic coupling vanishes as temperature approaches the transition temperature, so the dipole-dipole interaction potential experiences a rapid increase.

This increases the driving force promoting domain wall motion, but since the domain walls are pinned on defects, the magnetic tension in the system increases until it can overcome the pinning potential. Once this happens, the wall motion is rapid, as observed in Figure 3.9. One could call this a 'sling shot' mechanism.

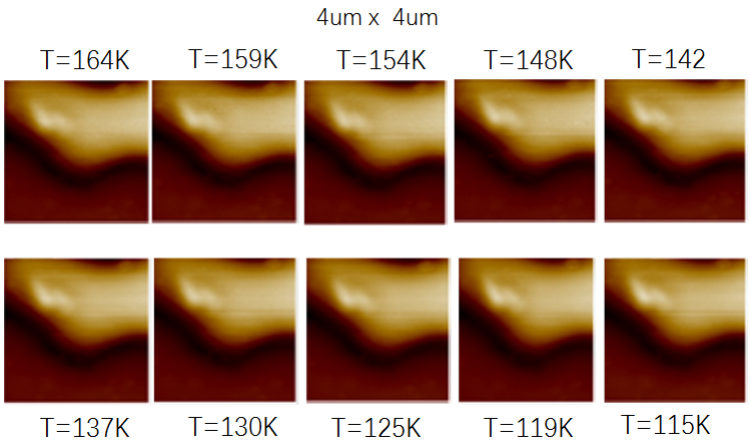

Figure 3.10: MFM images for the magnetic roughness measurement during zero field cooling.

3.3 Branching Domain Scheme

As introduced briefly in chapter one, there are various energy terms involved with magnetic domains, and competition between different energies is the reason for the formation of vastly diverse magnetic domain structures. Due to the complexity of magnetic materials, in order to accurately describe the magnetic domains one may have to resort to numerical solutions such as

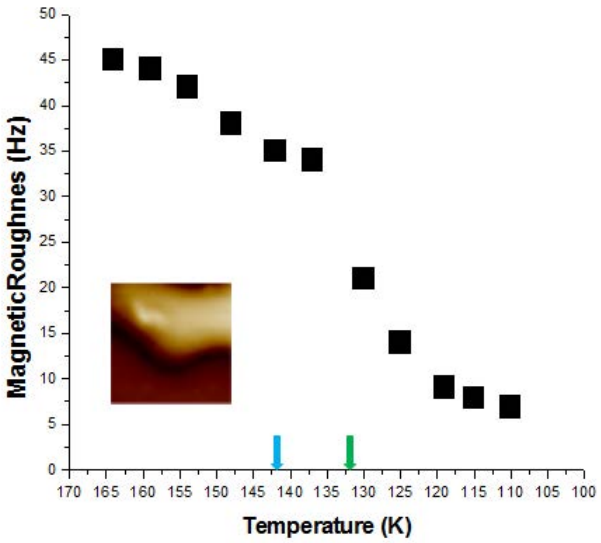

Figure 3.11: Magnetic roughness versus temperature, taken under zero-field-cooling conditions. The inset shows the area used for this measurement, which is labeled with a green box on the last image in Figure.3.9. Blue and green arrows label the temperature of the magnetic domain jump events discussed in Figure.3.9.

finite element method. Fortunately, for high anisotropy materials domain calculations can be simplified. UMn_2Ge_2 has been reported as a uniaxial high anisotropy material, so that with large enough sample size it is widely believed that its domain structure follows the branching domain scheme. This section will introduce the approximations that can be made with high anisotropy materials and compare the analytical calculations based on the branching domain scheme with the experimental data we acquired on UMn_2Ge_2.

3.3.1 μ^* Correction Approximation for High Anisotropy Materials

The calculation of the magnetic stray field energy is essential in magnetic domain theory. It has the general expression:

$$E_d = -0.5 \int_{sample} \vec{H}_d \cdot \vec{J} dV \tag{3.1}$$

In analogy with potential theory, one can introduce magnetic charges (volume charges and surface charges):

$$\lambda_v = -\nabla \vec{m} \tag{3.2}$$

$$\sigma_s = -\vec{m} \cdot \vec{n} \tag{3.3}$$

and the potential is:

$$\phi_d = \frac{J_s}{4\pi\mu_0}[\int \frac{\lambda_v(r')}{r - r'} dV' + \int \frac{\sigma_s(r')}{(r - r')} dS'] \tag{3.4}$$

The energy is the integral of the product of the magnetic charge and the potential:

$$E_d = 0.5 J_s[\int \lambda_v(r')\phi_d(r) dV + \int \sigma_s(r)\phi_d(r) dS] \tag{3.5}$$

However, the above formulas seem impractical as the field itself is generated by the magnetic charges and the distribution of magnetic charges is, in turn, affected by the field. In order to simply the model, the so called μ^* approximation method was developed. It assumes that the magnetization is

always aligned along the easy axis and that the stray field is not able to alter it too much, and any deviation can be treated as a perturbation and be taken into consideration in stray field calculation. Thus the magnetic charge distribution can be first calculated by using the unperturbed magnetization m_0, which follows the easy axis.

To introduce the correction from deviation, one define an effective permeability μ^*, and it is obtained by taking the second derivative of the anisotropy function along the easy axis. From it, one obtains a tensor, the diagonal component of it is (1,1+2K_d/g_1,1+2K_d/g_2), where $K_d = J_s^2/2\mu_0$ is a quantity related to saturation magnetization J_s. Particularly for uniaxial and cubic systems, coefficients g_1 and g_2 are equal, so that:

For cubic system:

Positive anisotropy:

$$\mu^* = 1 + \frac{K_d}{K_{c1}} \tag{3.6}$$

Negative anisotropy:

$$\mu^* = 1 - \frac{3K_d}{2K_{c1}} \tag{3.7}$$

For uniaxial system:

$$\mu^* = 1 + \frac{K_d}{K_u} \tag{3.8}$$

The approach is to calculate the stray field using the effective permeability:

$$\nabla \cdot (\mu_0 \mu^* \vec{H}_d) = J_s \lambda_v^0 \tag{3.9}$$

$$\vec{n} \cdot (\mu_0 \vec{H}_d^0 + \mu_0 \mu^* \vec{H}_d^i) = J_s \sigma_s^0 \tag{3.10}$$

Where the $\vec{H}_d^0$ and $\vec{H}_d^i$ are magnetic field outside and inside the boundaries. With calculated stray field, the energy becomes:

$$E_d = 0.5 J_s \int \vec{m_0} \cdot \vec{H}_d dV \tag{3.11}$$

Which now is much easier to calculate.

3.3.2 Two-Phase Domain Branching

For large size crystals, magnetic domains in the bulk and near the surface are very different. Firstly, the bulk domain tends to be relative simple and wide in order to save domain wall energy. Secondly, the surface domains could be very complicated and finer compared to the bulk in order to minimize the stray field or the closure field energy. One way to connect the surface and bulk domain structures is to use the concept of domain branching. Particularly, in a uniaxial material, domain branching follows a two-phase scheme, as shown in the Figure.3.12, which was first proposed by Lifshitz[37]. In the Two-Phase branching domain scheme the spins only have two possible orientations, and small domains grow inside big domains with opposite spin toward the surface. The total energies of this configuration involves consideration of mainly three energies: 1) Wall energy density that increases with branching towards the surface, 2) The field closure energy near the surface, and 3) Internal stray field energy. If we adopt the model in the Figure, the total energy per unit surface

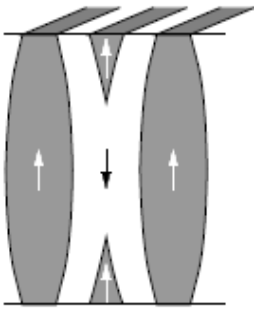

(a) Two-phase scheme of branching domains.

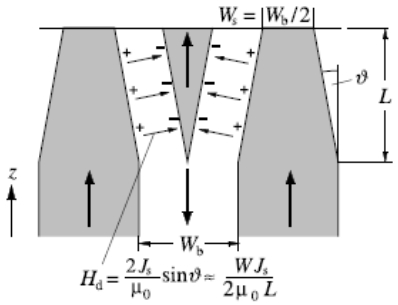

(b) A model for two-dimensional two-phase branching domains.

Figure 3.12: Schematics of branching domains and scheme of estimating the internal stray field for a one-generation branching process[38].

area can be summarized as:

$$etot = 2\int_0^{T/2} [a\frac{ew}{W(z)} + F_i(\frac{dW(z)}{dz})]^2 dz + 2C_s W_s \tag{3.12}$$

Where T is the thickness of the sample, e_w is the wall energy as introduced in chapter one. Applying the μ^* approximation, C_s and F_i for high anisotropy compound are factors having the following expressions:

$$C_s = 0.163K_d\frac{2}{(1+\sqrt{\mu^*})} \tag{3.13}$$

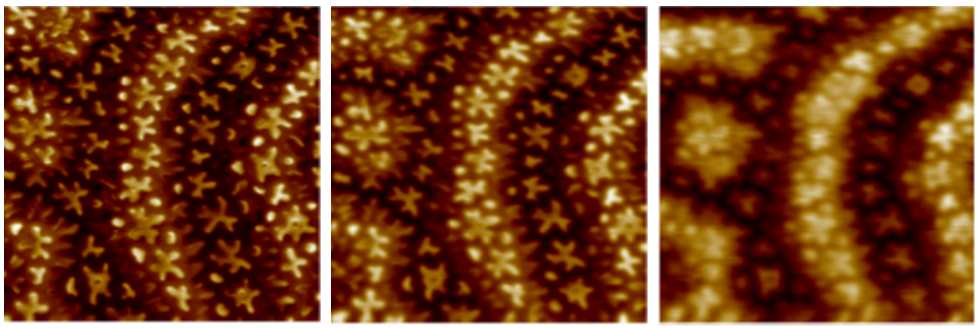

(a) 129nm (b) 390nm (c) 784nm

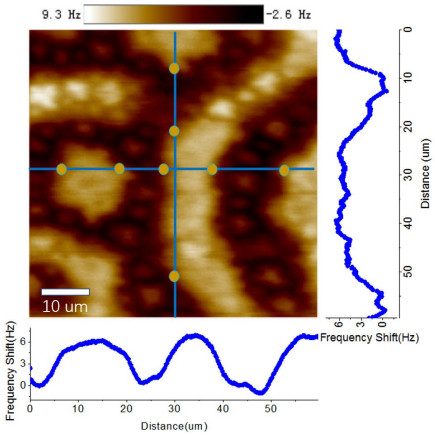

(d) 1049nm

Figure 3.13: Branching magnetic domains blur out when the lift scan height increases.

$$F_i = 0.5\frac{k_d}{\mu^*} \tag{3.14}$$

The latter expression is obtained by specifically using scheme in Figure.3.12(b). Clearly, there is a relation between the domain width W_b, W_s and the sample thickness T in order to minimize the energy. Similar to the domain wall energy calculation introduced in chapter one, one can approach this as a variational

problem, and thus obtain:

$$T = \sqrt{W_b^3 F_i/\lambda_w}[\arccos\sqrt{\omega} - \sqrt{\omega(1-\omega)}] \tag{3.15}$$

Here, $\omega = W_s/W_b$. If we take the approximation: $\omega \approx 0$, we get:

$$W_b = \sqrt[3]{(4/\pi^2)(\lambda_w/F_i)T^2} \tag{3.16}$$

and

$$W_s = 4\lambda_w F_i/C_s^2 \tag{3.17}$$

From the above equations, one gets:

$$W_b = \sqrt[3]{(4/\pi^2)(0.037W_s)T^2} \tag{3.18}$$

The magnetic domain pattern on UMn_2Ge_2 resembles the magnetic patterns reported on $NdFeB$, a high uniaxial anisotropy compound, which also appears to be flower-like. As stated, the UMn_2Ge_2 reported as a strong uniaxial anisotropy material, the pattern of magnetic domains on it should also follow the branching domains scheme. Namely, small volume of a branching domain grows on the surface inside the big domain stemming from the bulk. Figure 3.13(d) shows a room temperature scanning image with lift height around 1 um, where flowers like branching domain patterns disappeared at high altitude since its volume is small so that the intensity of generated stray field damps rapidly with distance. The large domains stay and exhibit a maze-like shape. Theoretically, using the high uniaxial anisotropy approximation, and only considering the branch scheme in two dimensions, the strip domain

width W_b, magnetic thin film thickness T, and branching domain width W_s should follow the equation.3.18 derived above. Our sample thickness is around 0.3mm, W_s is measured by averaging the width of branching domain which is about 1.8um, we obtained from the above equation, W_b=13.5um. On the other hand, experimentally, the strip domain width can be obtained by applying the speleological method:

$$W_b = \frac{2 * Total\ test\ line\ length}{\pi * Numberofintersection} \tag{3.19}$$

This is shown in Figure 3.13(d), where there are two test lines with intersections labeled by dots. This measurement gives us a value of $W_b \approx 10um$. Theory and experiment agree reasonable well considering the highly simplified two-dimensional approximation, thus supporting the branching domain scheme.

3.4 Exchange Constant and Saturation Magnetic Moment

As already introduced in Chapter one, domain wall width can be calculated by exchange coupling constant A and anisotropy energy. For uniaxial ferromagnetic materials, the magnetic domain wall width can be expressed specifically as:

$$\delta_w = 2\sqrt{A} \int_0^{\vartheta} \frac{d\theta}{\sqrt{k_1 \cos^2\theta + k_2 \cos^4\theta}} \tag{3.20}$$

k_1 and k_2 are the first and second order anisotropy constants, having published values of $1.57MJ/m^3$ and $19MJ/m^3$, respectively[31].

Experimentally, domain wall width can be directly measured by taking cross section on the boundary of two strip domains.

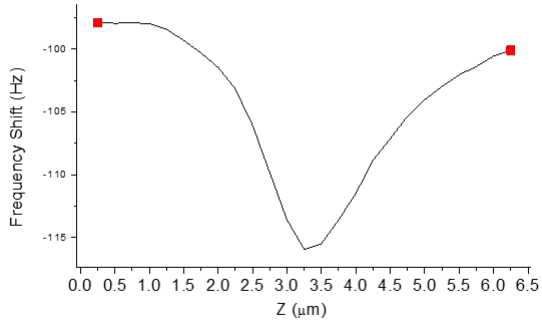

Figure 3.14: Domain Wall width measurement at T=87K.

Figure.3.14 shows a cross section of domain wall taken at temperature T=87K. Figure.3.15 shows numerical plot of the integral part in equation.3.20. According to Lilley's definition[39], as the Figure.3.15 shows, one takes the slope of the function at the center of the wall, and multiplies the rotation angle π to calculate wall width, that is the wall width is defined as $\delta_w = \sqrt{A}\pi k$, where k is the slope as marked in the figure. In order to find the exchange coupling constant A, we use the result of Figure.3.15 to fit our experimental data at Figure.3.14. Experimentally we found domain wall width is around 1.6 μm according to above definition. We thus obtained exchange coupling constant:

$$A = 4.8 \times 10^{-6} J/m \tag{3.21}$$

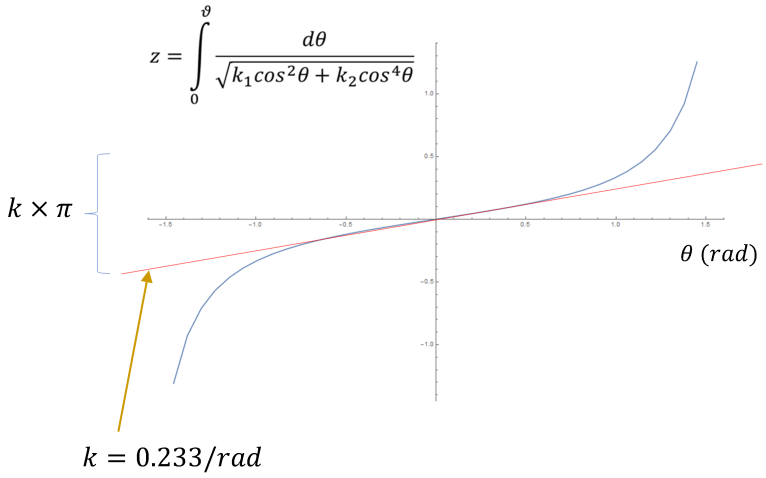

Figure 3.15: Wall width calculation.

This, of course, is a substantially larger quantity than typical exchange constant.

Further, from the above approximations and equations, the saturated magnetic moment J_s can be estimated by the following equation:

$$J_s = \sqrt{54\lambda_w \mu_0 / W_s} \tag{3.22}$$

Where domain wall energy density $\lambda_w = 32.2 J/m^2$ according to Equations.1.39, Equation.1.40 and experimental domain wall width. We calculated $J_s \approx 27 tesla$, much larger than that of $NdFeB$ about 1.6 $tesla$ [40].

We argue that these calculated values are upper limits. The reason is that above calculations are only available because of wall width measurement, however, domain wall below the sample surface such as the schematics in Figure.3.12 shows, may not be vertical to the surface, and cantilever generally

not only sensors the magnetic domains near surface but also is affected by magnetic features fairly below it. A tilting wall inside the crystal would effectively lead to a measurement broader than it should be. Thus the exchange coupling constant and saturation magnetization are overestimation based on the equations applied.

There are other factors need to addressed: first, it is true anisotropy constant and exchange coupling constant may effectively change with temperature. With our observation, cross section of domain wall doesn't change very much with temperature, which indicates that their counteracting roles in domain wall energy expression may have reduced the error of domain wall width brought by thermal agitation; second, the nature of magnetism in UMn_2Ge_2 is itinerant, Heisenberg model works as an effective theory.

As a rough estimation, the strong exchange coupling constant and saturation magnetization is consistent with the picture that UMn_2Ge_2 is a strong magnet.

3.5 Nature of 'Flowers'

3.5.1 In Plane Anisotropy

On the other hand, prominently, the flower shape of these branching domains and their orientations are not at all random, but highly self-similar, as can be seen by comparing different flowers in Figure.3.16 From the zero field temperature warming experiment in Figure.3.9, at low temperature the bright branching domains first only stretch into two primary directions approximately

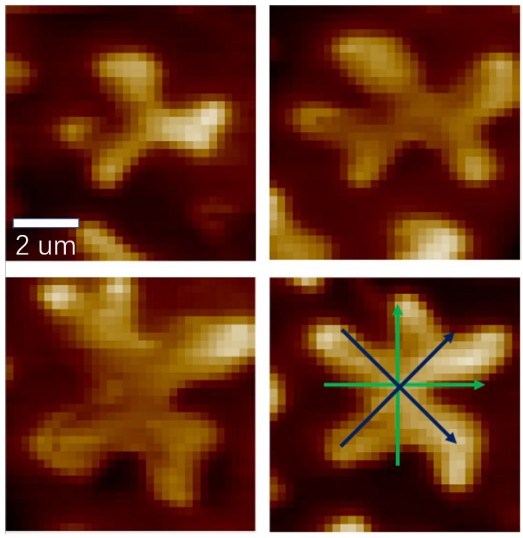

Figure 3.16: Flower pattern at a different position. The shape and orientation of the flower pattern turns out to be very self-similar. The branching domain walls align themselves into roughly 8 directions. The slight mismatch may have to do with competition from local closure field energy as well as distortion brought by scanner hysteresis.

perpendicular to each other. As the temperature increases, they break into smaller strips, and can switch from one direction to the other, and for higher temperature, these strips may choose a direction that is about 45 degrees with the primary direction. Since our sample size is macroscopic, larger than the usual dimensions when shape anisotropy starts to be important, this direction bias and evolution may strongly imply the existence of in-plane anisotropy which is contradictory to the assertion that UMn_2Ge_2's anisotropy is uniaxial.

First, as already mentioned for large size magnetic films the magnetic domain wall is of Bloch type[41], where the spin rotates in the plane of wall while it feels the in-plane anisotropy potential. A wall plane that is oriented

toward the in-plane potential minima will tend to have less energy cost. By examining each flower-like pattern, one can find 4 directions in which the branch domains initially grow, labeled green in Figure 3.16. Secondly, domain walls want to be parallel with each other when they become close in order to minimize dipole-dipole interaction, and sometimes this need can overcome in-plane anisotropy energy to follow 4 in-plane anisotropy secondary energy minima, labeled black in Figure.3.16. In addition to the examples in Figure.3.16, for any other pair of flower branching domains, one can always observe the trend following the above two mechanisms, which can be used to explain why all the flower-like domain patterns are similar shape and orientation.

3.5.2 Sub-domain Structure

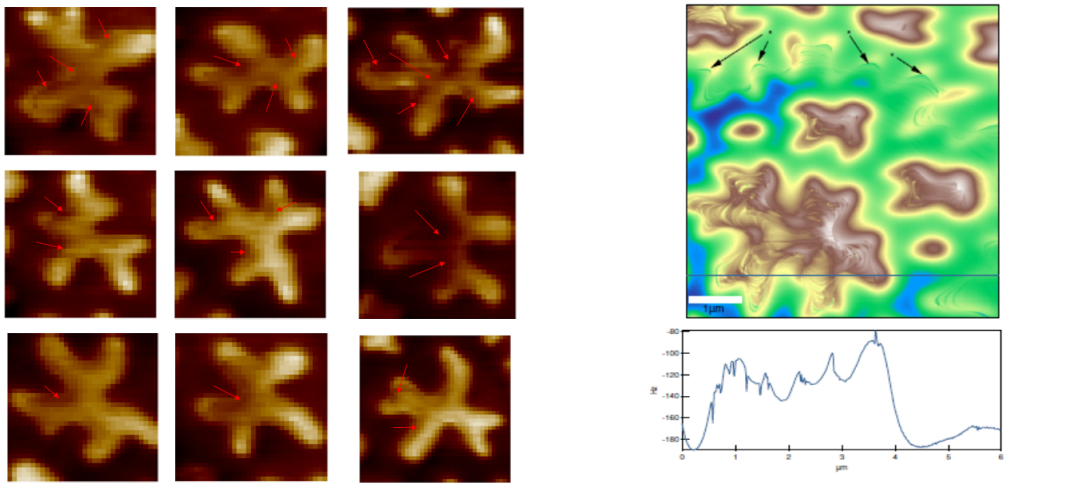

(a) Nanodomains on UMn_2Ge_2.

(b) Nanodomains on $NdFeB$ [42].

Figure 3.17: Small nano-domains have been observed in branching domains for both compound.

It is very interesting to notice that for many of the flower-like magnetic branching domains there are sub-structures inside. After examining the flower branching domains, it turns out that the MFM image for many domains is not smooth, there are lines of dark regions that sometimes trace the shape of the domains, as marked by red array in Figure 3.17(a). This phenomena is very much like what has been reported on the MFM image on a $NdFeB$ single crystal[42], in which lines of nano domains were investigated: an example is shown in Figure 3.17(b).

As stated previously, the cantilever we used has a low moment, but it is not ultra-sharp. This could be the reason why the small domains we observed are not as sharp as those on $NdFeB$. The highly similar features on both compounds strongly implies that the existence of more delicate nanodomains inside the branching domains could be a universal feature for all bulk magnetic crystals with high uniaxial anisotropy.

Chapter 4

Low Temperature Spin Polarized Scanning Tunneling Microscope Instrumentation

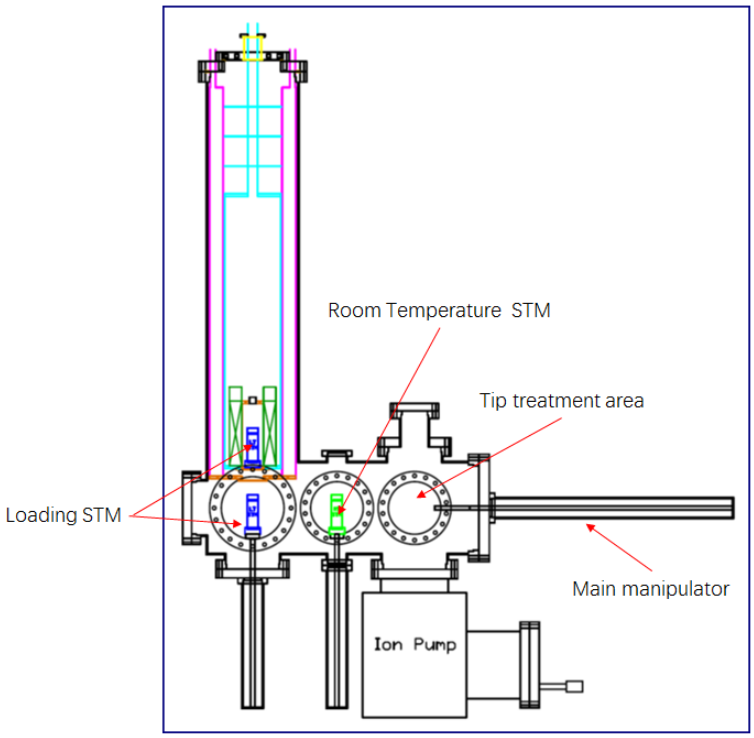

Figure 4.1: Schematics of LT-SP-STM.

The major difference between Spin Polarized Scanning Tunneling Microcopy and regular scanning tunneling microscopy, as mentioned in Chapter

one, is the magnetized tip. However, it must also can scan under external magnetic field. Our SP STM system incorporates high magnetic field and E-Beam Evaporation system, and the design guideline is to be compact and simple in design.

4.1 General STM design and In-situ Tip and Sample Transfer

In 1984, after the invention of the first STM at the IBM Zurich labs in Switzerland, a low temperature STM was demonstrated shortly thereafter at Stanford University[43]. After years of application, the approach to construct a LT STM is very well developed. However, integration of a superconductive magnet into the system is still challenging. The major difficulty is how to install the magnet properly, while keeping the STM tip and sample transfer simple.

Our LT-SP-STM fist takes advantage of a solenoid magnet to avoid extra intricacy in coil configuration, which greatly reduces the cost and substantially decreases the size of the system. In order to fit into the solenoid, the microscope body must be compact, with small diameter. Further, it must be detachable from the magnet as there is no space for tip and sample transfer inside the magnet. To substantially reduce the diameter of the STM, a modification to the traditional 'pan type' approach design was made. Instead of using stacks of shear-piezo plates as walker legs, a single piezo-plate was used as shown in the Figure. This piezo moves a rectangular piece of a silicon wafer

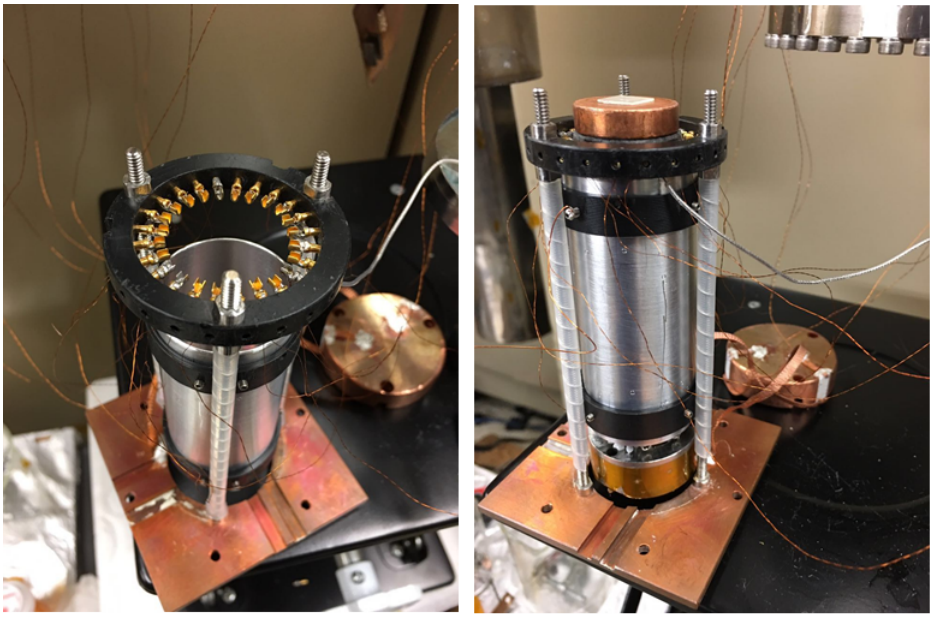

Figure 4.2: STM and the STM rack.

coated with silicon nitride up and down, and the shaft for the z-walker slides on it with small graphite pads touching the silicon nitride. Since the silicon nitride is made with standard semiconductor technology, it is extremely flat and smooth. Also, the physical and chemical properties of silicon nitride are ideal for sliding. There are total of six walker legs. Three of them press against three symmetric points at the top of the z-walker slider and the other three at the bottom. While most of the walker legs are fixed to the STM body by screws, at the top and bottom, separately, there is one leg specially designed so that it presses against the z-walker slider by adjustable leaf springs. This controls the friction between the legs and the z-walker slider and holds together the whole microscope structure. Figure 4.5 below shows the STM body

once everything is assembled.

Since the STM must have a removable design, a ring as illustrated in Figure 4.2 was placed inside the magnet that is designed to hold the weight of the STM and provide electrical contacts at the same time. The STM can be loaded and unloaded onto the support ring from the bottom of the magnet.

The details of the electrical contacts are as follows. First, for the STM, there are total 24 flexible phosphor bronze wires with a diameter of 15 mils installed into a machined Delrin head on the top of the microscope. This connects to all the functional parts on the STM body, serving as a connector to the outside controllers and sensors. The phosphor bronze wires match 24 female pins facing up like "cups" on the support ring as the Figure shows. The support ring is held by three vertical rods. A copper heatsink at the top of the whole structure is thermally connected to the bottom of the Helium dewar by a copper strap; it serves to add weight on top of the STM to improve the electrical contacts, as well as serving to cool the STM rapidly.

To transfer the tip and sample, the procedure is to simply lift the STM a little and rotate the STM so that the phosphor bronze wires clear the female cups. Then it can be pulled out easily from the bottom of the dewar and into the chamber space for tip and sample transfer. Though this is a very compact and simple design for a LT-SP-STM, it suffers from deficiencies other STMs may not have. First and foremost, after tip or sample transfer, the STM must be reconnected to the support ring. Even though the phosphor bronze wire is quite flexible at ambient conditions, its resilience might degrade at low

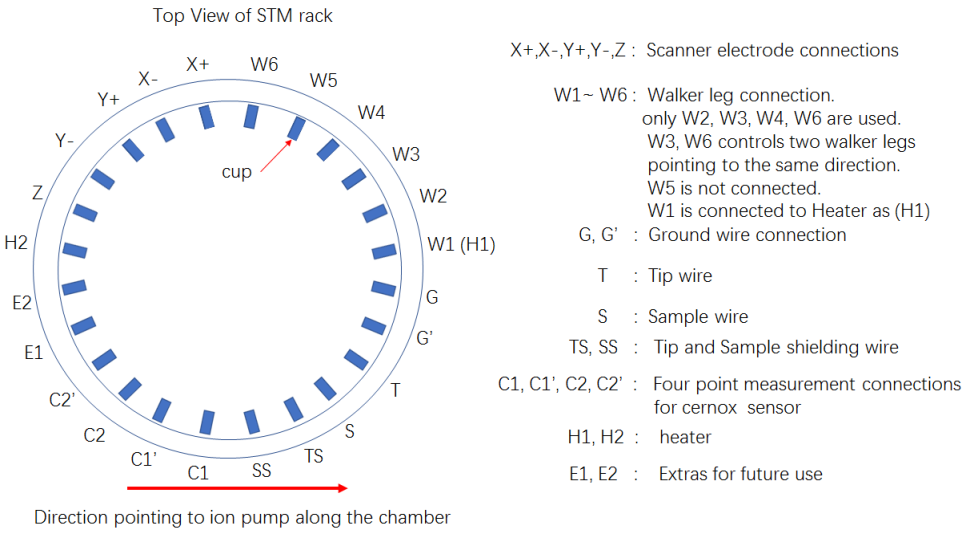

Figure 4.3: Schematics of 'cup' connections.

temperature, so it is not easy to make all 24 pins have good contact at the same time, and this brings extra intricacy to the operation. Second, once the STM is pulled out, the STM is exposed to room temperature radiation heat, and the STM body temperature will rise rapidly, yet cooling inside the dewar is slow. Moreover, even with a short exposure, a very cold sample may get rapidly contaminated, thus requiring for higher vacuum standard in the main chamber. In addition, one must check all contacts every time the STM is loaded into place. The scanner and walker legs can be measured by capacitance, the Cernox temperature sensor can be determined by a digital multi-meter diode measurement, and the heater by resistance. But, the grounding wire, tip and sample wire contacts cannot be directly measured. The initial design was to use two independent wires connecting all the away to the STM (only for the tip,

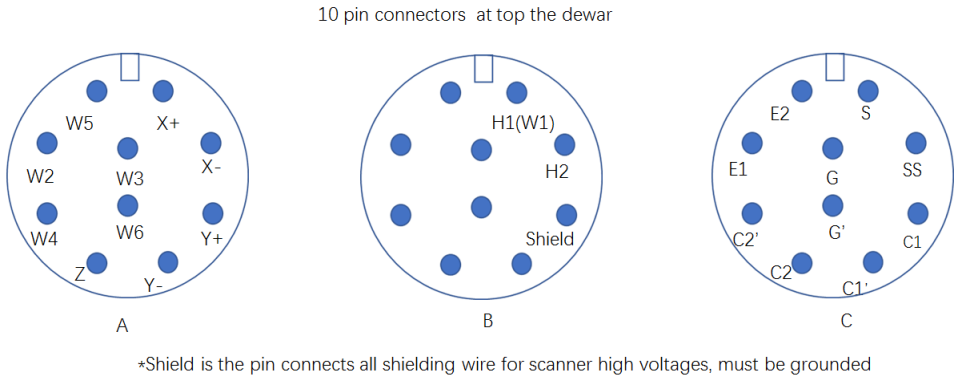

Figure 4.4: Schematics of 10 pins connectors on top the dewar.

sample and ground). One just needs to check the continuity of the connections to make sure the contact is good. However, this design uses excessive wires and occupies more connecting ports. As mentioned above, it may be cumbersome to have both pins make contact only for checking one connection. Therefore, a particular trick was developed. We modified the sample stage as Figure 4.5 shows. A golden pin was designed to attach to the sample stage and bent beneath the bottom of the tip stage. In order to check contact of tip and sample connections the scanner is walked down, approaching this gold pin with feedback on, so it stops when the tip stage connects to sample stage through the golden pin. Next time, when loading STM, one simply needs to check continuity between sample and tip to check if the contact is ok. Since the tip wire is coaxial and there are two silver epoxy joints at the connector on the top flange of the dewar and one at the cup, the total resistance when both tip and sample wire are in good contact is about 40 ohm. This design avoids

the need of extra wires for connection verification purpose after tip or sample transfer. Also it provides a reference point to sense the distance between tip and sample when STM is in operation.

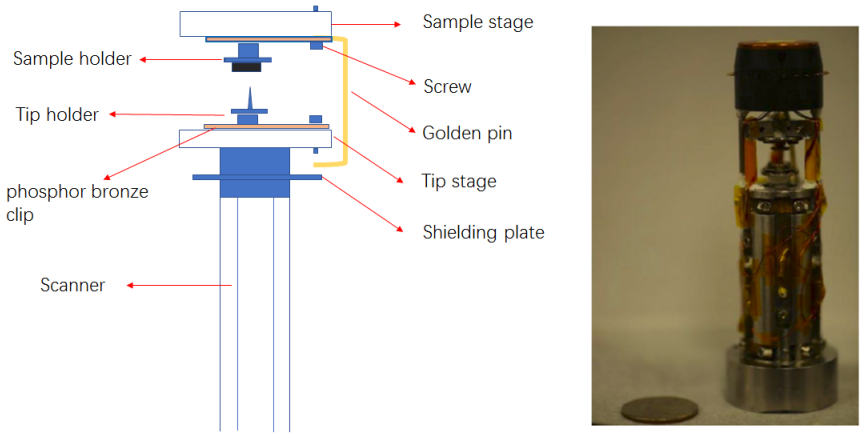

Figure 4.5: The golden pin and STM body.

4.2 Grounding and Shielding

Shielding is very important for protecting the tunneling area from disturbances caused by electromagnetic waves. As the chamber is very well grounded, the STM inside is shielded well from EM waves outside the chamber. However, there are other EM wave sources inside the chamber that need to be taken care of.

First, the scanner is sometimes subjected to high and rapidly changing voltages, so this must be shielded very well from the tunneling area. The top of the scanner is a Macor plate serving as insulation, a grounded aluminum

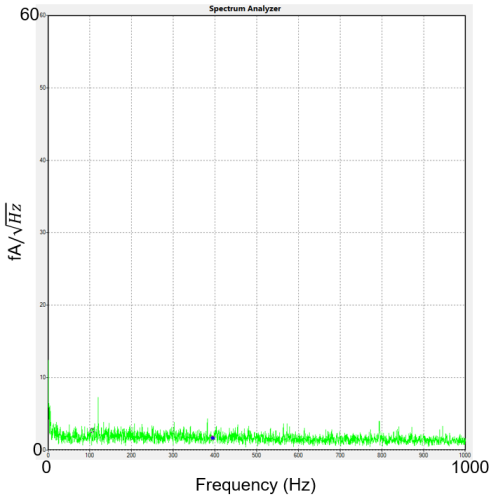

Figure 4.6: Low noise level as shown in spectrum analyzer without tunneling, the 60Hz noise is completely removed.

plate is mounted on top of it to provide shielding between the tip stage and the scanner. The jacket outside the scanner is grounded as well, and the wires connecting the scanner are further shielded by grounding coils when passing the tunneling area to the Delrin head. Second, in order to provide shielding from other signals such as the Cernox sensor, heater and scanner/walker wires connecting the cups to the outside of the inner dewar, a grounded aluminum pipe is installed covering the tunneling area as the Figure.4.2 shows. For wire shielding, the tip wire is a coax specifically designed for low temperatures, and the sample wire is shielded by twisting it with a grounded wire.

Avoiding grounding loops is another issue to be taken care of, mainly to eliminate 60Hz noise. When the STM is scanning all equipment that shares grounds with the chamber such as the ion gauge, walker control circuit, turbo

and roughing pumps, and so on, must be turned off and unplugged from the outlet. The ion pump grounding wire is removed from the plug, as it shares the ground with the chamber. The only ground that connects to the outlet is the STM controller, the ion pump and chamber are grounded through preamplifier cable to the controller and to the outlet. Thus only one ground path exists for the whole system. The 60 Hz noise is thus eliminated in our system.

4.3 Vibration Isolation

As the figure shows, the chamber system hangs on a wooden frame that is supported by three granite pillars. Wood is preferred over metal because it has better damping characteristics. Each pillar weighs about 1000 pounds, composing a very low resonant frequency vibration system, thus filtering low and high frequency noise. A pneumatic isolator is placed under each pillar serving as extra buffer, typically inflated to a pressure of about 80 PSI. The chamber hangs from the wood frame at only two points: one is a screw at the top of the outer dewar, and the other is a stainless steel cable near the other end of the chamber. The inner dewar has a soft bellow structure above the top flange, thus if necessary the inner dewar can be suspended using this bellow, partially isolating it from the chamber. The bellow also provides a small freedom to adjust the position of the inner dewar so that it does not touch the inner wall of the outer dewar, which is essential for preventing bubbling noise from the outer dewar.

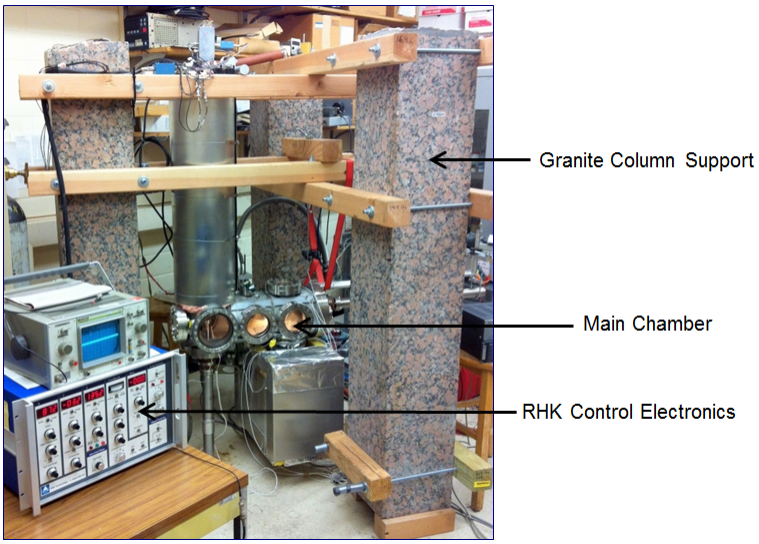

Figure 4.7: STM system supporting structure[44].

4.4 Tip Treatment and E-beam Evaporation Stage

Most STM experiments use tungsten tips, because of their high rigidity, high melting point and because they are easy to etch into a sharp point. However, the tip can easily oxidize in air leading to unstable tunneling. In order to remove the oxidation, we use high voltage electron bombardment on the apex. On the heating stage there are two filaments with this purpose.

For spin polarized tunneling, we also need to coat the tip with magnetic materials. A primitive e-beam evaporator is integrated into the heating stage. There are two filaments installed for heating a cobalt rod by electron bombardment to the point of evaporation. The tip can be placed between the cobalt rod and another filament, the latter is for heating the tip holder to help obtain uniform cobalt deposition.

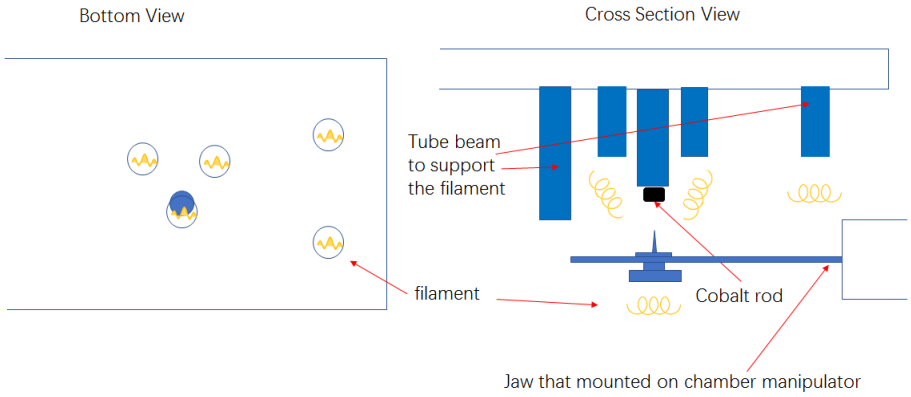

Figure 4.8: Tip treatment stage inside the chamber treatment area as indicated in the figure 4.1.

4.5 In Situ Sample Cleaver

The scanning tunneling microscope is a surface probe technique requiring atomically flat, ultra-clean working surfaces. For low temperature STM, this usually necessitates in-situ sample cleaving in high vacuum. There has been a great amount of methods to cleave samples with different advantages and disadvantages. The most popular one is mounting a stud such as an aluminum piece with epoxy on top of the sample, and then knocking it off inside the chamber. The stud takes away part of the sample, leaving a cleaved surface on the sample holder. However, it is often difficult to apply epoxy uniformly, and the position of the cleaving plane cannot be determined in advance. For hard materials, the cleave may fail because the epoxy joint breaks. Another more traditional method is to use a blade to cut the sample. It generally solves the above problems but needs some extra design as the cutting must

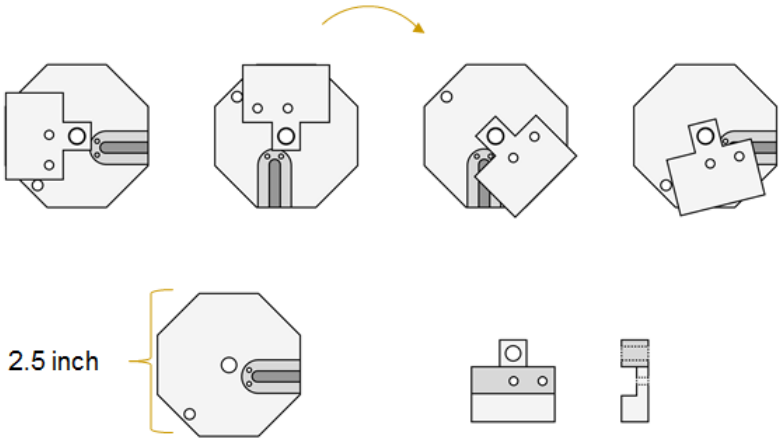

Figure 4.9: Schematics of the cleaver. It consists of a 'hammer' on which the blade is mounted, and the hammer is able to rotate on the plate where sample holder resides. There is a catcher on the plate to hold the position of the hammer initially before cleaving. The plate is attached to load lock manipulator and stay fixed, and the hammer is able to rotate around the manipulator once released from catcher and cut the sample on the plate.

be performed inside vacuum. There are quite a lot cleaver machines as well, some of them are of rather delicate design that may require a certain amount of labor to machine, while others occupy significant space inside the chamber. To solve this problem, a very simple cleaver design was developed that uses gravity for the cleaving force. It consists of only two parts as sketched in that are very easy to machine and assemble, fitting well our current experimental setup. The motion of cleaving is controlled by only one rotational degree of freedom, so it can be attached to the rotary load lock manipulator in our system and it is removable when not in use, saving chamber space. With the help of this small gadget, we have successfully cleaved the bilayer manganite

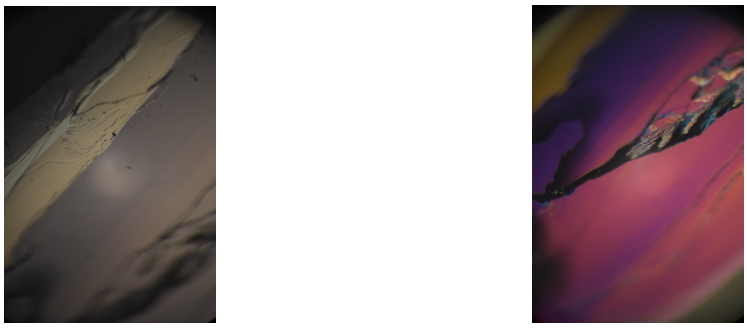

Figure 4.10: Cleaved surface of $La_{2-2x}Sr_{1+2x}Mn_2O_7$ with x=0.5 under optic microscope, the right hand side used polarized light.

sample with mirror like atomic flat surface.

4.6 Crash Site on HOPG with Atomic Resolution

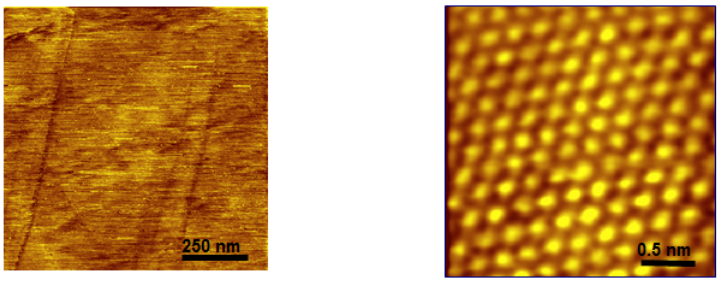

Figure 4.11: Topography and atomic resolution of graphite.

SP-STM is still an on going project. Though atomic resolution with spin polarized tunneling hasn't yet been realized. Atomic images are achieved both on graphite and bilayer manganite with non-magnetic tip such as Figure.4.11 and Figure.4.12 show.

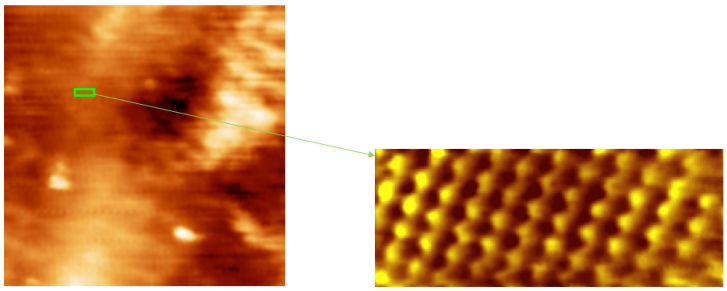

Figure 4.12: Atomic resolution of bilayer manganite $La_{2-2x}Sr_{1+2x}Mn_2O_7$ with x=0.5.

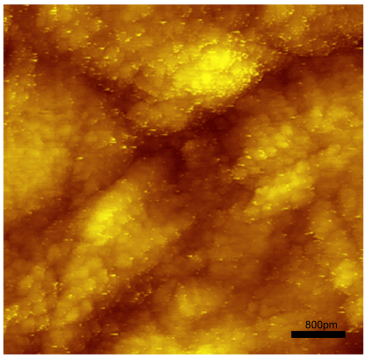

Figure 4.13: Crash scene on graphite with atomic resolution.

During scanning on graphite, a particular interesting event is observed. A discharge event happened in ion pump which we assume shortly disturbed the feedback loop. Fast action of scanner caused vibration and random motion of the STM tip, which pierced into the graphite and broke many bonds in the HOPG lattice. Luckily, the STM tip immediately after the crash still preserve the atomic resolution capability and the crash scene was observed in ultra-high solution as the figure 4.12 shows, possibly this is the first illustration of atomic

resolution images of a crack on graphite.

Bibliography

[1] G. Binnig and H. Rohrer Rev. Mod. Phys. **59(3)**, 615, (1987).

[2] G. Binnig, C. F. Quate, and Ch. Gerber Phys. Rev. Lett. **56(9)**, 930, (1986).

[3] Roland Wiesendanger Rev. Mod. Phys. **81**, 1495, (2009).

[4] Franz J. Giessibl Rev. Mod. Phys. **75**, 949, (2003).

[5] A. Wadas and P. Grtter Phys. Rev. B. **39**, 12013, (1989).

[6] $www.ntmdt - si.com/data/media/files/spm_basics$

[7] Hartmann U Annual Review of Materials Research, **29**, 53-87, (1999).

[8] J. Tersoff and D. R. Hamann Phys. Rev. Lett. **50**, 25, (1983).

[9] Alex Hubert and Rudolf Schafer Magnetic Domains: The analysis of magnetic microstructures Springer-Verlag Berlin Heidelberg **106** (1998).

[10] Alex Hubert and Rudolf Schafer Magnetic Domains: The analysis of magnetic microstructures Springer-Verlag Berlin Heidelberg **201** (1998).

[11] G. Meyer and N. M. Amer Appl. Phys. Lett. **53**, 1045 (1988).

[12] C. W. Yuan, E. Batalla, M. Zacher, and A. L. de Lozanne, Appl. Phys. Lett. **65**, 1308 (1994).

[13] A. Volodin, K. Temst, C. Van Haesendonck, and Y. Bruynseraede, Rev. Sci. Instrum. **71**, 4468 (2000).

[14] C. Israel, C. Hyun, A. de Lozanne, S. Phark, and Z. G. Khim, Rev. Sci. Instrum. **77**, 023704 (2006).

[15] Y. Seo, P. Cadden-Zimansky, and V. Chandrasekhar, Appl. Phys. Lett. **87**, 103103 (2005).

[16] Seongsoo Kweon, Nitin Samarth, and Alex de Lozanne Journal of Applied Physics. **105**, 093906 (2009)

[17] Tien Ming Chuang, Alex De Lozanne Review of Scientific Instruments **78**, 053710 (2007)

[18] Tien-Ming Chuang, PhD Dissertation, University of Texas at Austin, (2008)

[19] Lieberman, Michael A.; Lichtenberg, Allan J. Principles of plasma discharges and materials processing (2005)

[20] Ronald Hoffmann and Chong Zheng, J. Phys. Chem. **89**, 4175 (1985).

[21] Marianne Rotter, Marcus Tegel, and Dirk Johrendt Phys. Rev. Lett. **101**, 107006 (2008)

[22] Jiangang Guo, Shifeng Jin, Gang Wang, Shunchong Wang, Kaixing Zhu, Tingting Zhou, Meng He, and Xiaolong Chen Phys. Rev. B. **82**, 180520(R) (2010)

[23] Z. Fisk, D. W. Hess, C. J. Pethick, D. Pines, J. L. Smith, J. D. Thompson, and J. O. Willis, Science **239**, 33 (1988)

[24] H. H. Hill and B. T. Matthias, Phys. Rev. **168**, 464 (1968).

[25] A. J. Dirkmaat, T. Endstra, E. A. Knetsch, A. A. Menovsky, G. J. Nieuqenhuys, and J. A. Mydosh, J. Magn. Magn. Mater. **84**, 143 (1990).

[26] R. Movshovich, M. Jaime, S. Mentink, A. A. Menovsky, and J. A. Mydosh, Phys. Rev. Lett. **83**, 2065 (1999).

[27] A. M. Boring, R. C. Albers, G. H. Schadler, A. C. Lawson, P. Weinberger, and N. E. Christensen, Phys. Rev. B **36**, 5507 (1987).

[28] A. Szytula, S. Siek, J. Leciejewicz, A. Zygmunt, and Z. Ban, J. Phys. Chem. Solids **49**, 1113 (1988).

[29] P. P. J. van Engelen, D. B. de Mooij, and K. H. J. Buschow, IEEE Trans. Magn. **24**, 185 (1988).

[30] R. D. Kirby, J. X. Shen, J. A. Woollam, and D. J. Sellmyer, J. Appl. Phys. **69**, 4574 (1991).

[31] David S. Parker,Nirmal Ghimire, John Singleton, J. D. Thompson, Eric D. Bauer, Ryan Baumbach, David Mandrus, Ling Li, and David J. Singh Phys. Rev. B. **91**, 174401 (2015).

[32] Junwei Huang, Changbae Hyun, Tien-Ming Chuang, Jeehoon Kim, J. B. Goodenough, J.-S. Zhou, J. F. Mitchell, and Alex de Lozanne Phys. Rev. B **77**, 024405 (2008)

[33] Morgann berg, PhD Dissertation, University of Texas at Austin, (2014)

[34] A. Hubert, W. Rave and S. L. Tomlinson Phys. stat. sol. (b) 204, 817 (1997).

[35] W. Rave, E. Zueco, R. Schafer, A. Hubert Journal of Magnetism and Magnetic Materials 177-181 (1998) 1474-1475.

[36] S.F. Matar, J. Etourneau Journal of Alloys and Compounds **275-277** (1998) 468-471

[37] E. Lifshitz J. Phys. USSR **8**, 337C346 (1944)

[38] Alex Hubert and Rudolf Schafer Magnetic Domains: The analysis of magnetic microstructures Springer-Verlag Berlin Heidelberg **314** (1998)

[39] B.A. Lilley Phil. Mag. (7) **41**, 792C813 (1950)

[40] $https://en.wikipedia.org/wiki/Neodymium_magnet$

[41] Charles Kittel Reviews of Modern Physics **21** 541 (1949)

[42] Lunan Huang Valentin Taufour, T. N. Lamichhane, Benjamin Schrunk, Sergei L. Budko, P. C. Canfield, and Adam Kaminski Phys. Rev. B. **93**, 094408 (2016).

[43] S. A. Elrod, A. L. de Lozanne, and C. F. Quate Appl. Phys. Lett. **45**, 1240 (1984)

[44] Seong Heon Kim and Alex de Lozanne Review of Scientific Instruments. **83**, 103701 (2012)